machines

MDPI

Article

Design-Orientated Optimization and Motion Planning of a Parallel Platform for Improving Performance of an 8-DOF Hybrid Surgical Robot

Asna Kalsoom [1], Muhammad Faizan Shah [2,*], Zareena Kausar [1], Faizan Khan Durrani [3], Syed Zahid Hussain [4] and Muhammad Umer Farooq [1,*]

[1] Institute of Mechanical & Manufacturing Engineering, Khwaja Fareed University of Engineering & Information Technology, Rahim Yar Khan 64200, Pakistan; asnakalsoom8@gmail.com (A.K.); zareena.kausar@kfueit.edu.pk (Z.K.)
[2] School of Information Technology and Systems, Faculty of Science & Technology, University of Canberra, Canberra, ACT 2617, Australia
[3] Iman Group, Islamabad 44000, Pakistan; faizankhandurrani92@gmail.com
[4] Department of Mechatronics Engineering, Air University, Islamabad 44000, Pakistan; szahidhussain@au.edu.pk
* Correspondence: faizan.shah@canberra.edu.au (M.F.S.); umer.farooq@kfueit.edu.pk (M.U.F.)

Abstract

The emergence of surgical robots has revolutionized complex operations, improving precision, lowering operating risks, and shortening recovery periods. Given the merits, an eight degrees of freedom (DOF) hybrid surgical robot (HSR) has been proposed, which leverages the benefits of both serial and parallel manipulators. However, its performance is hindered by the constrained range of motion of its parallel platform. To address the issue, this research presents a systematic approach for designing and optimizing the proposed HSR. The first step is the design of the HSR, followed by a multi-stage design analysis of its parallel platform, concentrating on kinematic, geometrical, and singularity analysis. Higher values of the condition number indicate singular configurations in the platform's workspace, highlighting the need for an optimized design. For optimization of the platform, performance parameters like global condition number (GCN), actuator forces, and stiffness are identified. Initially, the design is optimized by targeting GCN only through a genetic algorithm (GA). This approach compromised the other parameters and raised the need for simultaneous optimization employing a non-dominated sorting genetic algorithm (NSGA II). It offered a better trade-off between performance parameters. To further assess the working of the optimized parallel platform, workspace analysis and motion planning of a predefined trajectory have been performed.

Keywords: hybrid surgical robot; design optimization; genetic algorithm; non-dominated sorting genetic algorithm

check for updates

Academic Editor: Xinjun Liu

Received: 8 October 2025
Revised: 3 November 2025
Accepted: 8 November 2025
Published: 9 November 2025

Citation: Kalsoom, A.; Shah, M.F.; Kausar, Z.; Durrani, F.K.; Hussain, S.Z.; Farooq, M.U. Design-Orientated Optimization and Motion Planning of a Parallel Platform for Improving Performance of an 8-DOF Hybrid Surgical Robot. *Machines* **2025**, *13*, 1038. https://doi.org/10.3390/machines13111038

Copyright: © 2025 by the authors. Licensee MDPI, Basel, Switzerland. This article is an open access article distributed under the terms and conditions of the Creative Commons Attribution (CC BY) license (https://creativecommons.org/licenses/by/4.0/).

1. Introduction

In the field of medicine, surgery is one of the most essential treatments that provides diagnosis and cure for various injuries, traumas, and pathological issues through operative procedures [1]. The emergence of robotic technology in the surgical fields has revolutionized the way challenging procedures are carried out, enhancing precision, lowering operating risks, and shortening recovery periods. Since their development in the late 20th century, surgical robots have undergone tremendous evolution, providing improved

capabilities that exceed the constraints of human dexterity, precision, and consistency [2]. Recent developments, including the integration of artificial intelligence, have further enhanced these technologies to include real-time data analysis and semi-autonomous surgical functions. These robots are designed in order to help surgeons perform minimally invasive surgeries (MISs), which save patients from discomfort, reduce incision sizes, and speed up their recuperation periods [3].

The design or architecture of surgical robots plays a crucial role in their performance, which has been divided into three categories, i.e., serial robots, parallel robots, and hybrid robots [4,5]. Among these three, serial robots are utilized frequently. They are made up of a chain-like structure consisting of multiple connected segments, which enables a broad range of motion and precise placement of tools and end effectors. One of the most readily available serial robots is the da Vinci Surgical System, which was first introduced in the early 2000s [6]. Some other serial surgical robots presented in the literature include Neuroarm [7], the Sehance Surgical System [8], Mirosurge [9], Raven [10], and Versius [11], which have proved their potential in MISs but have drawbacks including reduced stiffness and high inertia [12].

Parallel manipulators, on the other hand, offer high precision and stiffness as well as compactness, positional accuracy, rigidity, and high payload to weight ratio. Due to these benefits, they are employed in various medical applications like guiding spinal pedicle screws placement, drill guiding for distal locking screws in intramedullary nailing, endoscopic ventriculostomy, hip arthroplasty, etc. [13]. A parallel manipulator designed for orthopedic surgeries includes a six degrees of freedom (DOF) fixator [14] and MBARS [15]. Similarly, a parallel robot was proposed by [16] facilitating skull surgeries, a micro-robot for ophthalmic surgeries was designed by [17], and the parallel robot named MARS was described in [18] for spinal cord procedures. Despite all the benefits, the use of parallel manipulators is limited due to their constrained workspace, but newer models and designs are still being proposed for expanding the span of their applications in surgical fields [19].

Hybrid surgical robots (HSRs) seek to address these shortcomings by combining both parallel and serial architectures, providing a well-balanced solution that refines both operating scope and precision [20]. They are made to carry out a variety of surgical procedures with exceptional precision and dependability, ensuring motion in multiple dimensions [21]. Moreover, these are suitable for a variety of surgical operations, especially those that call for minimal invasiveness and great precision [18]. Given these merits, a hybrid robot named PARASURG 5M was proposed, with its detailed kinematic and dynamic modeling, as a viable solution for MIS by [22]. Another robot was designed, consisting of two modules: the PARAMIS robot and the serial position module. It provided the required motion control and in-depth workspace analysis for different surgical limitations and applications [23]. A 3-DOF parallel manipulator combined with a single-DOF prismatic joint was described in [24]. A 5-DOF hybrid manipulator was designed and optimized on the basis of global performance index (GPI) using a pattern search method targeting spinal cord MIS [25]. A study reported a multi-DOF HSR using two bendable serial segments consisting of parallel universal joint-based bending linkages, which aimed for the manipulation of soft tissues with a positional accuracy error of below 1.2 mm [26]. For the treatment of spinal and orthopedic conditions, an 8-DOF HSR was configured using linear actuation and PID control [27]. For changing the position and orientation of the tools, a 7-DOF hybrid mechanism was introduced. It was a combination of a 4-DOF SCARA and a 3-DOF (2R1T) parallel wrist [28]. Another study presented by [29] put forward a concept of a 4-DOF HSR based on haptic response for laparoscopic surgeries. For dental implants, a parallel platform-based 5-DOF hybrid robot was designed and optimized based on neural networks. The optimization algorithm targeted the limited workspace of the parallel platform by minimizing

its joint displacements [30]. A miniature palm-sized HSR has been introduced recently for ophthalmic surgeries based on a double five-bar mechanism, a decoupled ball joint, and a tool cartridge mechanism [30]. Both HSRs and parallel surgical manipulators have experienced major improvements in recent years. For example, the authors in [31] have performed a kinematic study of multiple redundant parallel mechanisms in orthopedic fracture reduction surgery, finding a design with significantly better tilting. On the same note, ref. [32] not only optimized a 3-DOF parallel robot platform to perform laparoscopic surgery of the pancreas but also employed sophisticated genetic algorithms to ensure that the resulting system was highly precise and had a big workspace, which was conducive to complex anatomy. Detailed reviews regarding hybrid parallel–serial manipulator systems also emphasize the revived enthusiasm to combine the benefits of serial and parallel mechanisms (high stiffness, accuracy, and big workspace) in modern designs [4]. The researchers in [33] have demonstrated a new 3PUS-PRU parallel mechanism module attached to a 6-DOF hybrid machine, which indicates that parallel mechanisms are innovative and can be used in contemporary hybrid robots. Mentioning such current studies on parallel and hybrid machines will be more helpful to set the context and the originality of the proposed research, as suggested by the reviewer. Motivated by the effectiveness of the HSRs for several surgical procedures, an 8-DOF miniaturized HSR has been proposed in this paper.

The proposed HSR consisting of a 6-DOF parallel platform and a 2-DOF serial manipulator leverages the potentials of both mechanisms, but its weakness lies in the confined range of motion of the parallel platform, which has a closed-loop architecture. This drawback limits the dexterity of the HSR, reduces its precision, and risks the mobility of the robot by limiting its reach to deep or complicated anatomical surgical sites. Consequently, surgeons are compelled to reorient the robot extensively at the expense of the HSR's performance, resulting in longer surgery duration, enhanced procedure complexity, and possible decreases in surgical precision. To overcome this drawback, this research aims to analyze the design of the HSR's parallel platform through multi-stage analysis and optimization of the parallel platform's design based on three crucial performance parameters.

The multi-stage analysis focuses on three different analyses, including kinematic analysis, geometrical analysis, and singularity analysis. These analyses highlight the limitations of the HSR's parallel platform and form the basis for its design optimization. After the platform's optimization, evaluation of its workspace was carried out. Finally, the optimized model of the HSR's parallel platform is tested for its motion-planning abilities for a predefined 3D trajectory. To the best of the authors' knowledge, this study is the first in the field of HSRs that provides a detailed multi-stage analysis of the HSR's parallel platform followed by its design optimization through two different optimization approaches. The article is structured in the following manner. The detailed description of the HSR's design is provided in Section 2. The following Section 3 discusses the multi-stage analysis of the HSR's parallel platform. The design of the platform has been optimized in Section 4. Motion planning of the optimized platform has been analyzed in Section 5. The results of this study have been thoroughly discussed in Section 5 followed by the conclusion in Section 6.

2. The HSR's Architecture

This section gives the virtual representation of the HSR, explaining how its components are attached. The design of the HSR mainly consists of two distinct parts: a 6-DOF parallel manipulator and a 2-DOF serial manipulator. The purpose of the parallel platform is to approach and aim for the position of interest in the human body, whereas the serial manipulator handles and adjusts the position and orientation of the surgical tool. In this way, both components of the HSR help the surgeon in performing the surgical procedure

swiftly and efficiently. Figure 1 illustrates the design of the HSR with its labeled components. All the dimensions of the HSR, including the lengths of the links, angle between joints, radii of top and bottom plates, etc., are listed in Table 1. These parameters play a crucial role in designing the HSR and have a huge impact on its performance.

Table 1. Dimensions of the HSR.

Part Name	Dimension
Base Radius of Serial Manipulator (c)	7 mm
Serial Manipulator Link 1 (l1)	20 mm
Serial Manipulator Link 2 (l2)	20 mm
Lower Plate Radius (R)	30 mm
Upper Plate Radius (r)	20 mm
Upper/Lower Plate Thickness (w)	15 mm
Actuated Leg Length (L1)	45 mm
Upper Plate Joint Angles (α)	30°
Lower Plate Joint Angles (β)	60°

For upper and lower plates joint angles distribution, check Figure 2.

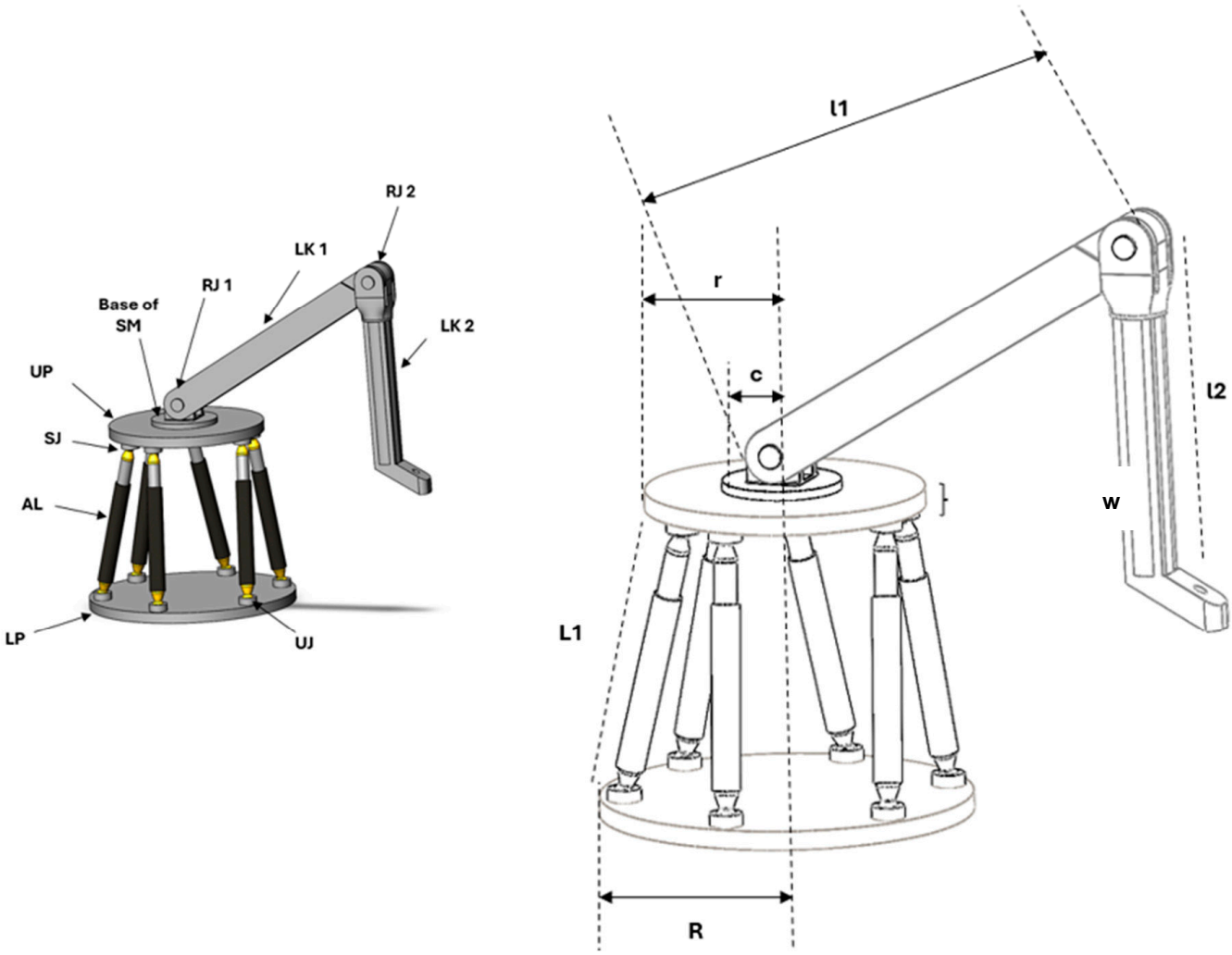


Figure 1. Design of the HSR with a description of all components. LP: Lower platform; UJ: universal joints; AL: actuated leg; SJ: spherical joint; UP: upper platform; SM: serial manipulator; RJ: revolute joint; LK: link.

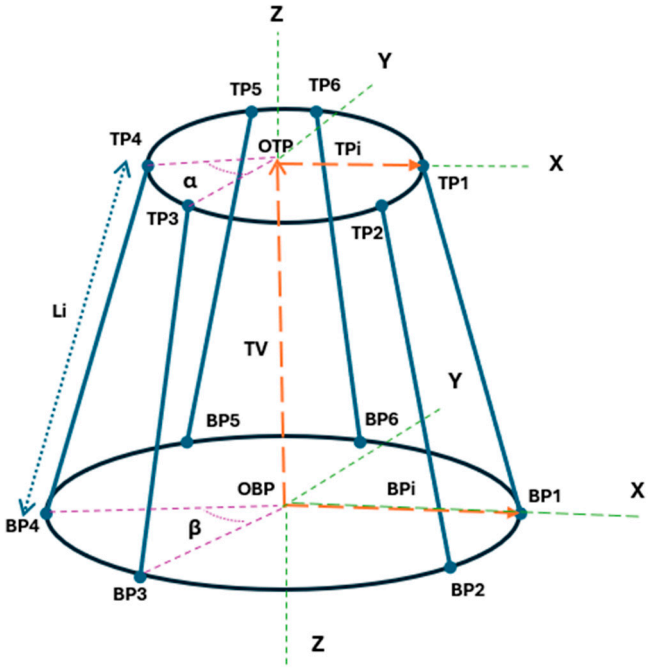


Figure 2. Vector diagram of the HSR's parallel platform depicting position vectors, frame of reference, and distribution of joints on top and bottom plates.

2.1. Two-Link Serial Manipulator

The 2-link serial manipulator of the HSR, also known as a robotic arm, is designed to facilitate two independent DOFs for enabling precise motion of the manipulator. The serial linkage is formed by the combination of two rigid links, which are interconnected in a series formation directly connected to the top plate of the parallel platform, designed to aim for the target position and configuration. Due to its connection with the top plate of the parallel platform, its motion is strictly coupled with this movable platform. The motion in the parallel platform also results in the motion of the serial manipulator while reorienting its frame of reference. The serial manipulator will now perform the task in the redefined frame of reference and work volume while maintaining synchronization with the parallel platform. It is the part of the surgical robot that also contains a tool post or tool guide for the attachment of the surgical tool. This serial manipulator is designed to be lightweight but structurally rigid and stable with minimal inertia and adequate mechanical strength.

The main components include two rigid links, revolute joints, linear actuators, a fixed base, and an end effector interface. The connection between the HSR's parallel platform and the base of the serial manipulator is supported by a base revolute joint, which is the first actuated joint of the serial linkage. This base joint enables the first DOF of rotational motion by joining the first rigid link to the base. This first link acts as the fundamental component in the motion of the serial manipulator, as it transmits motion to the second rigid link of the manipulator. At the intersection of both rigid links, there is an elbow revolute joint, which is responsible for the second DOF. The second link is further extended to the end effector interface, which is the point of tool attachment. When the top plate of the parallel platform moves, the actuated joint between the plate and the first link also initiates the motion of the serial manipulator. This motion is then transferred to the second rigid link, which finally moves the tool in the desired direction to perform the desired task by the surgeon. In this way, the flexible yet robust structure of the serial manipulator executes the minimally invasive surgical tasks precisely and smoothly. Figure 1 shows the assembly of the components of the 2-link serial manipulator of the HSR.

2.2. Parallel Platform

This parallel platform is similar to a hexapod in design since it contains six actuated links/legs and is well known for its high stiffness and stability [34]. Moreover, the design consists of two upper and lower plates, universal joints, ball and socket joints, and linear actuation. The legs are attached between these plates at a certain angle using both kinds of joints. This particular design of parallel platform facilitates a total of six DOFs, i.e., three rotational motions and three translational motions.

The compact structure of the parallel platform is designed so that the bottom plate serves as the fixed foundation of the entire structure, and the legs are attached to it through universal joints at a specific angle. Essentially, these universal joints are attached to the base plates at specific angles relative to each other, determining the position of the links/legs on the plate, as depicted in Figure 1. These joints facilitate the smooth and jerk-free tilt of the actuated legs and also ensure safety from undesired torsional stress. The top plate is the movable platform, which is directly in contact with the serial manipulator. It is supported by the six actuated legs attached to it using ball and socket joints or spherical joints. These spherical joints enable an unhindered multi-dimensional tilting and rotation of the top movable plate. The motion is primarily driven by six linear actuators attached to each leg, which produce an independent motion for each leg. The closed-loop control of the system ensures the synchronization of the motion of each actuator. Linear actuation is preferred in the case of the HSR due to its benefits like high precision, high torque, and smooth control [35]. In this way, the compact and robust structure of the parallel platform provides support and stability for the serial manipulator as well as the whole HSR, helping the surgeons perform their intended surgical procedures with precision.

3. Multi-Stage Design Analysis

In order to understand the motion of a manipulator, its kinematic, geometrical, and singularity analyses are crucial, which provide insights into its position, velocity, and singularities. Inverse kinematic analysis helps in determining the leg/link lengths of the parallel manipulator, which are required to achieve the desired pose. Similarly, the geometrical and singularity analyses aid in estimating the singularities and workspace constraints of the robotic system utilizing the Jacobian matrix. For providing a comprehensive understanding of the HSR's parallel platform's motion and singularities, these three analyses have been carried out in this section.

3.1. Kinematic Analysis

Kinematic analysis or kinematic modeling is the evaluation of a manipulator's motion without considering the forces that caused it. This analysis is concerned with analyzing the geometric aspects of the motion, position, trajectory, velocity, and acceleration of the manipulator. Among forward and inverse kinematic analysis, solving inverse kinematics for parallel manipulators is simpler because the solution becomes complicated due to higher-order non-linear equations in the case of forward kinematics [36]. Estimating the link lengths and joint angles when the final position and orientation of the end effector is known is termed as inverse kinematics [37]. In this study, the inverse kinematic analysis has been carried out for the parallel platform of the proposed surgical robot. For this purpose, a MATLAB® (version 2023) code has been designed using analytical equations of the inverse kinematics and required link lengths have been computed for the desired position.

The position of the manipulator requires a relationship between input and output parameters. The output parameters are the link lengths and the angles between these links while the input parameters comprise three rotational motions and three translational motions along the X, Y, and Z axes. To simplify the analysis, all six links of the HSR's

platform were assumed to be identical, and the results were computed for i^{th} link of the platform. The results obtained from this analysis were integrated along all six links of the platform. Figure 2 depicts the vector diagram of the parallel manipulator, which helps in understanding the kinematic modeling of the platform. T_{Pi} and B_{Pi} (where $i = 1, 2, \ldots, 6$) are the position vectors defining the position coordinates of each link on the top and bottom plate with respect to the reference frame; L_i represents the i^{th} link of the platform, TV is the translation vector, which has a standard form of $[x\ y\ z]^T$; O_{BP} and O_{TP} are the central points of the bottom and top plates, respectively, where the frames of reference for both plates have been defined; and H_i refers to the resultant vector that is obtained from the head to tail rule of vector addition.

By using geometric relations and vector addition theorem, the link length L_i for the i^{th} link is calculated as presented in Equation (1).

$$L_i = TV + {}^{P}_{B}RT_{Pi} - B_{Pi} \tag{1}$$

$${}^{P}_{B}R = R_Z(\psi)R_Y(\theta)R_X(\phi) \tag{2}$$

$${}^{P}_{B}R = \begin{pmatrix} \mathrm{c}(\psi)\mathrm{c}(\theta) & -\mathrm{s}(\psi)\mathrm{c}(\phi)+\mathrm{c}(\psi)\mathrm{s}(\theta)\mathrm{s}(\phi) & \mathrm{s}(\psi)\mathrm{s}(\phi)+\mathrm{c}(\psi)\mathrm{s}(\theta)\mathrm{c}(\phi) \\ \mathrm{s}(\psi)\mathrm{c}(\theta) & \mathrm{c}(\psi)\mathrm{c}(\phi)+\mathrm{s}(\psi)\mathrm{s}(\phi)\mathrm{s}(\theta) & -\mathrm{c}(\psi)\mathrm{s}(\phi)+\mathrm{s}(\psi)\mathrm{s}(\theta)\mathrm{c}(\phi) \\ -\mathrm{s}(\theta) & \mathrm{c}(\theta)\mathrm{s}(\phi) & \mathrm{c}(\theta)\mathrm{c}(\phi) \end{pmatrix} \tag{3}$$

$$T_{Pi} = \begin{bmatrix} rcos\alpha & risn\alpha & 0 \end{bmatrix}^T \tag{4}$$

$$B_{Pi} = \begin{bmatrix} Rcos\beta & Rsin\beta & 0 \end{bmatrix}^T \tag{5}$$

$$TV = \begin{bmatrix} 0 & 0 & a \end{bmatrix}^T \tag{6}$$

where R is the rotation matrix from O_{BP} to O_{TP} and has been explained by Equations (2) and (3), TV is the translational vector defined by elevation a in the Z axis, and T_{Pi} and B_{Pi} are joint position vectors for the upper and lower plates, respectively. In these equations, r represents the radius of the movable top plate, R is the radius of the fixed bottom plate, c and s represent cosine and sine, respectively, and ψ, θ, and ϕ denote Euler angles in their respective axis.

Figure 2 also explains the angle distribution of joints on both the top and bottom plates. All six universal joints on the bottom plate are equally distributed at an angle β of 60 degrees. Similarly, on the top plate, each adjacent pair of spherical joints is separated by an angle α of 30 degrees. This configuration ensures uniform load distribution, enhanced kinematic isotropy, structural stability, and minimal coupling effects between actuators in the HSR's parallel platform [38]. The joint angle distribution also facilitates the computation of position vectors T_{Pi} and B_{Pi} (where $i = 1, 2, \ldots, 6$) for each link of both the upper and bottom plates, respectively, as described in Equations (4) and (5). The final equations computing the link lengths of the HSR's platform are:

$$L_1 = \begin{pmatrix} rc\psi c\theta - R \\ rs\psi c\theta \\ a - rs\theta \end{pmatrix} \tag{7}$$

$$L_2 = \begin{pmatrix} 0.866rc\psi c\theta - 0.5rs\psi c\phi + 0.5rc\psi s\theta s\phi - 0.5R \\ 0.866rs\psi c\theta + 0.5rc\psi c\phi + 0.5rs\psi s\theta s\phi - 0.866R \\ a - 0.866rs\theta + 0.5rc\theta s\phi \end{pmatrix} \tag{8}$$

$$L_3 = \begin{pmatrix} -0.5rc\psi c\theta - 0.866rs\psi c\phi + 0.866rc\psi s\theta s\phi + 0.5R \\ -0.5rs\psi c\theta + 0.866rc\psi c\phi + 0.866rs\psi s\theta s\phi - 0.866R \\ a + 0.5rs\theta + 0.866rc\theta s\phi \end{pmatrix} \tag{9}$$

$$L_4 = \begin{pmatrix} -0.866rc\psi c\theta - 0.5rs\psi c\phi + 0.5rc\psi s\theta s\phi + R \\ -0.866rs\psi c\theta + 0.5rc\psi c\phi + 0.5rs\psi s\theta s\phi \\ a + 0.866rs\theta + 0.5rc\theta s\phi \end{pmatrix} \tag{10}$$

$$L_5 = \begin{pmatrix} -0.866rc\psi c\theta + 0.5rs\psi c\phi - 0.5rc\psi s\theta s\phi + 0.5R \\ -0.866rs\psi c\theta - 0.5rc\psi c\phi - 0.5rs\psi s\theta s\phi + 0.866R \\ a + 0.866rs\theta - 0.5rc\theta s\phi \end{pmatrix} \tag{11}$$

$$L_6 = \begin{pmatrix} rs\psi c\phi - rc\psi s\theta s\phi - 0.5R \\ -rc\psi c\phi - rs\psi s\theta s\phi + 0.866R \\ a - rc\theta s\phi \end{pmatrix} \tag{12}$$

The HSR's parallel platform uses the above estimated link lengths when aiming for a particular desired pose. These link lengths are fed as inputs to the linear actuators of the platform, which will generate the motion required to reach the target position. Any deviation in these values may lead to positional inaccuracies and errors in the platform's performance.

3.2. Geometrical Analysis

Kinematic modeling is essential for establishing a relation between the manipulator's link displacements and end effector's position and orientation. This analysis helps in controlling the manipulator in its feasible workspace. But, along with the manipulator's link displacements and orientation, another key parameter that governs the performance of the manipulator is its velocity. In order to control the position and force of the manipulator, determining its angular velocity and wrench values is important. For calculating these parameters, a Jacobian matrix is developed, which depends upon the configuration of the robot [39]. The Jacobian matrix provides a relationship between the rate of change of joint position over time with linear and angular velocities of the end effector. It plays a significant role in motion planning, force balancing, and ensuring precision of the manipulator. The Jacobian matrix of the HSR's platform has been derived utilizing Equation (1) by taking its derivative with respect to time.

$$\dot{L}_i = \left(\dot{TV} + {}^P_B\dot{R}\ T_{Pi} - \dot{B_{Pi}} \right) \tag{13}$$

Since the base attachment is fixed from the base, B_{Pi} becomes zero and the Equation (13) reduces to:

$$\dot{L}_i = \dot{TV} + {}^P_B\dot{R}\ T_{Pi} \tag{14}$$

The angular velocity ω of the HSR is related to the term ${}^P_B\dot{R}$ by a relation ${}^P_B\dot{R} = S(\omega){}^R_BR$, where $S(\omega) = \begin{bmatrix} 0 & -\omega_z & \omega_y \\ \omega_z & 0 & -\omega_x \\ -\omega_y & \omega_x & 0 \end{bmatrix}$. Integrating this relation in Equation (14) yields:

$$\dot{L}_i = \dot{TV} + S(\omega){}^R_BRT_{Pi} = \dot{TV} + \omega \times {}^R_BRT_{Pi} \tag{15}$$

Using the same logic, the linear velocity $\dot{T}_{Pi}$ of the upper spherical joint can be determined as:

$$\dot{T}_{Pi} = \dot{TV} + \omega \times r_{Pi}, \quad where\ r_{Pi} = {}^R_B R\ T_{Pi} \tag{16}$$

The actuator elongation rate is the projection of this spherical joint velocity along the actuator's direction vector S_i, defined as a unit vector from the base joint B_{Pi} to the upper joint T_{Pi}. This direction vector S_i can also be defined as:

$$S_i = \frac{L_i}{||L_i||} = \frac{T_{Pi} - B_{Pi}}{L_i} \tag{17}$$

Projecting the velocity $\dot{T}_{Pi}$ along the actuator's unit direction vector S_i gives the relation for the instantaneous velocity of the parallel platform's i^{th} actuator.

$$\dot{L}_i = S_i^T \left(\dot{TV} + \omega \times r_{Pi} \right) \tag{18}$$

For all six actuators, Equation (18) can be written as:

$$\dot{L}_i = \begin{bmatrix} S_i^T \\ S_2^T \\ \vdots \\ S_6^T \end{bmatrix} \dot{TV} + \begin{bmatrix} (S_1 \times r_1)^T \\ (S_2 \times r_2)^T \\ \vdots \\ (S_6 \times r_6)^T \end{bmatrix} \omega \tag{19}$$

Equation (19) can be further described in terms of translational and rotational sub-Jacobians J_t and J_r, respectively.

$$J_t = \begin{bmatrix} S_i^T \\ S_2^T \\ \vdots \\ S_6^T \end{bmatrix}, \quad J_r = \begin{bmatrix} (S_1 \times r_1)^T \\ (S_2 \times r_2)^T \\ \vdots \\ (S_6 \times r_6)^T \end{bmatrix} \tag{20}$$

Hence, Equation (21) gives the final Jacobian equation, which explains the relationship between the rate of change of joint position over time with linear and angular velocities of the end effector.

$$\dot{L}_i = \begin{bmatrix} J_t & J_r \end{bmatrix}_{J \epsilon 6 \times 6} \begin{bmatrix} \dot{TV} \\ \omega \end{bmatrix} = J \begin{bmatrix} V_{Px} \\ V_{Py} \\ V_{Pz} \\ {}^{P}_{B}\omega_x \\ {}^{P}_{B}\omega_y \\ {}^{P}_{B}\omega_z \end{bmatrix} \tag{21}$$

This matrix J serves as the fundamental parameter when estimating the condition number of the platform, which in return determines the singularities and workspace limitations of the platform. For precise and smooth motion of the platform, an accurate geometric model is highly important.

3.3. Singularity Analysis

In a robot's workspace, there are some configurations where it faces a loss of control or mechanical stiffness. In other words, the robot loses its DOFs, and when this happens, it may become uncontrollable. These configurations are termed as singularities in a robot's workspace and can be identified with the help of the Jacobian matrix [40]. When the determinant of the matrix becomes zero, it becomes singular, indicating that the robot has approached a singular configuration. The rank of the Jacobian matrix can also determine the singular configurations. The parallel mechanism of the HSR's platform faces many potential challenges due to its limited workspace and singularities. As the platform moves to perform surgical tasks, it may reach a configuration at which it loses its DOFs, indicating that the platform's Jacobian matrix has become rank deficient [41]. To avoid this issue, the singularity analysis based on the condition number is performed.

3.3.1. Condition Number

The condition number assesses the performance of a parallel manipulator by quantifying how well the Jacobian matrix maps the joint space to the Cartesian space, affecting key

parameters like velocity, acceleration, force, etc. [42]. It also plays a vital role in determining the singular configurations in a robot's workspace. The condition number $k(J)$ can be termed as the ratio between the largest singular value σ_1 to the smallest singular value σ_n of the Jacobian matrix. The value of the condition number varies between one and infinity. For an ideal robotic mechanism, the condition number should be close to unity. In the practical scenario, a lower condition number indicates that the robot is performing well and is free from distortions and errors. In the case of a high condition number, there are higher singularities in the robot's workspace, increasing the inaccuracies in its kinematic and dynamic behavior. Mathematically, it is expressed as:

$$k(J) = \frac{\sigma_1}{\sigma_n} \tag{22}$$

For gaining a complete understanding of the distribution of $k(J)$, the global conditioning number (GCN) is studied. The *GCN* is used to evaluate the robot's performance throughout its entire feasible workspace [43–45]. Mathematically, it is computed as the average condition number over various discrete points within the robot's workspace.

$$GCN = \frac{\sum_{i=1}^{n} k(J_i)}{n} \tag{23}$$

Here, n is the total number of discrete points that make up the workspace of the robot and $k(J_i)$ represent the condition number for i designs of the parallel platform. The purpose of the *GCN* is to determine the kinematic conditioning of the manipulator and quantitatively assess the sensitivity of end effector movement to the variation of the input to the actuators. As defined in Equation (23), the *GCN* is based on the Jacobian matrix (J) that defines the relationship between the velocities of the actuators and the end effector, and it is mathematically given as the ratio of the maximum and the minimum singular values of J throughout the manipulator's workspace. The values of the robot's *GCN*s are also bound between unity and infinity. Lower values of *GCN* indicates a well-conditioned manipulator, which has minute and negligible performance errors, while higher values of *GCN* leads to a faulty and unstable manipulator, which may have significant singularities. Consequently, the *GCN* is a critical parameter for identifying and avoiding singular configurations and for the evaluation of the overall motion reliability of the robotic system. In the present study, minimization of the *GCN* ensured that the optimized parallel platform maintained preferable manipulability and smooth movement over its working space, a prerequisite to precision surgical operations.

3.3.2. Singularity Analysis of the Parallel Platform

The singularity analysis provides quantitative information of the kinematic robustness of the HSR's parallel platform by evaluating the sensitivity of actuator displacement responses to the infinitesimal perturbations in platform pose. As discussed earlier, Jacobian matrix J bridges a relation among the platform's actuator rate vector $\dot{L}$ and platform twist vector $\dot{p}$ through $\dot{L} = J\dot{p}$. When J is rank deficient, small end effector positional changes may result in enormously large actuator efforts, introducing uncontrollability with respect to certain degrees of freedom, i.e., kinematic singularities. To model this behavior, the singularity analysis of the HSR's platform has been carried out at different configurations by altering the geometric parameters, like joint angles of both the upper and lower plates and the radii of both plates. Changes in the condition number and GCN were observed for each case to explore the behavior of the robot at different orientations. Four tests were conducted by changing the geometric parameters of the HSR's platform. Each test involved the rotation of the upper movable plate along three principal axes, i.e., X, Y, and

Z, constrained by angular restrictions for all three Euler angles of the platform: $\pm 30^\circ$ for ϕ, $\pm 60^\circ$ for θ, and $\pm 60^\circ$ for ψ, respectively.

A Latin hypercube sampling (LHS) scheme was used to generate 150 unique platform orientational configurations that are equally spaced throughout the selected Euler angle space. This large number of poses ensured a statistically representative coverage of the entire orientation space while limiting computational cost. LHS facilitates a quasi-uniform exploration of multi-dimensional spaces without clustering near particular poses so that both nominal and extreme configurations relevant for surgical operations are included. For each sampled pose, lengths of the actuators were calculated from the inverse kinematic model, and a numerical Jacobian was determined using central finite differences on the vector of leg lengths with respect to each of the six pose variables. This methodology directly captures the sensitivity and eliminates symbolic inconsistencies of the analytical Jacobian methodology.

The pose variables corresponded to a combination of angular displacements along all three axes, specifically covering displacements at two extreme values other than zero position (e.g., -60, 0 and +60). For each pose, the corresponding Jacobian matrices, condition numbers $k(J)$, and GCNs were computed to analyze the platform's singularities. The four test cases are mentioned below.

- **Case I:** The angles between the joints of the upper and lower plates were varied. The radii of both plates were different.
- **Case II:** The angles between the joints of the upper and lower plates were varied. The radii of both plates were the same.
- **Case III:** The angles between the joints of the upper and lower plates were the same. The radii of both plates were different.
- **Case IV:** The angles between the joints of the upper and lower plates were the same. The radii of both plates were the same.

Figure 3 displays the variation of k(J) for the 150 sampled poses of each case. A few significant conclusions can be made regarding this singularity analysis of the HSR's parallel platform:

- Case I has the lowest average condition number, which represents the best global dexterity among all four cases. The non-uniform radii of the plates create a slight variation in the orientation of the legs that increases the spatial distribution of the actuation directions by preventing near-parallel orientations of the legs. The variation of $k(J)$ in the range from 40 to 150 highlights the fact that it is an ill-conditioned manipulator.
- Case II has higher values of $k(J)$, peaking above 250, and indicates that plate radii equal but offset anchor angles, diminish the isotropy, and cause some partial leg collinearity in some orientations. The GCN (169.24) graph shows that this geometry is more likely to become ill-conditioned when the platform is tilted towards extreme orientations.
- Case III is in a significantly worse condition, with $k(J)$ being exceedingly over 300. The imbalance between upper and lower plate radii causes various lines of actuators to become more crowded in similar space directions, creating near-singular situations and less dexterity. This degradation is affirmed by the average GCN = 291.56.
- Case IV is the worst conditioned formation. If the two radial axes are equal and offsets are the same, the leg pattern is made almost symmetric, and during some positions, many leg axes tend to be coplanar. This is what leads to a $k(J)$ of more than 500 in several instances of the poses, resulting in a very high GCN value of 401.08. The resultant large condition numbers suggest that, for even small end effector displacements, large uneven actuator extensions would be needed, which are not desirable in precision surgical motion.

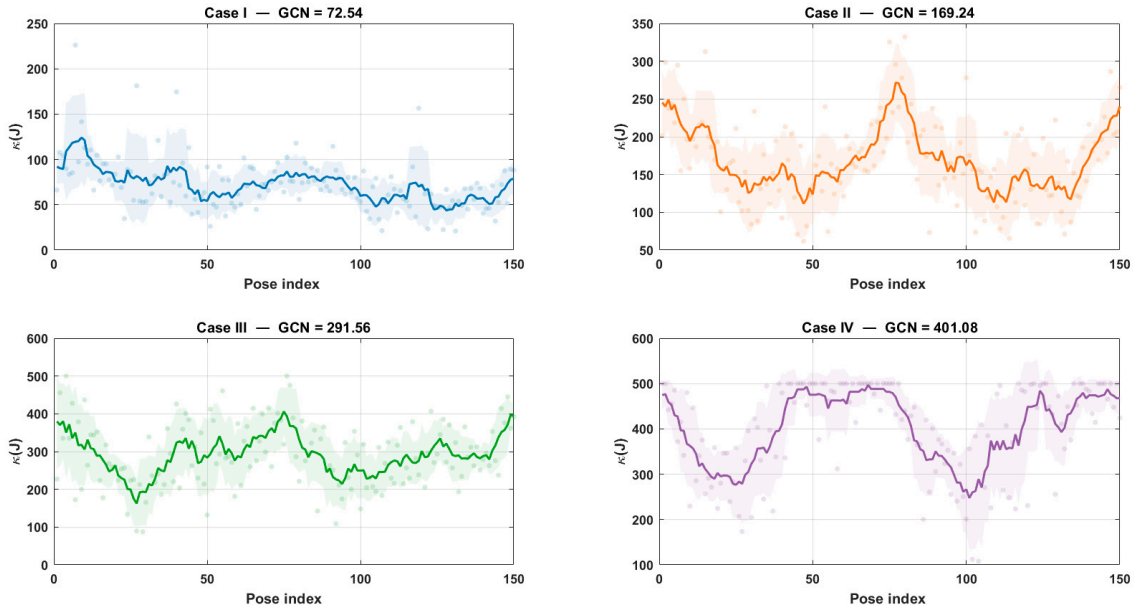


Figure 3. Distribution of condition numbers for four test cases. **Case I**: Different joint angles and different upper and lower plate radii. **Case II**: Different joint angles and same upper and lower plate radii. **Case III**: Same joint angles and different upper and lower plate radii. **Case IV**: Same joint angles and same upper and lower plate radii.

An increasing GCN trend is observed from Case I to Case IV, which is depicted in Figure 4 and Table 2, a fact that proves the geometric sensitivity of the platform conditioning as the combination of symmetric offset and that equal plate radii increases the violation of kinematic isotropy of the manipulator. The dispersal of values of $k(J)$ over 150 poses further demonstration that poor conditioning does not only occur in rare poses but over very broad areas in the space of maneuvers in surgery, suggesting that it is very easy for the system to fall into nearly singular configurations while executing typical maneuvers in general surgical practices. The large GCN values obtained (>>1) suggest that none of the four geometrical configurations offer isotropic enough behavior to ensure good force or motion control. High condition numbers are associated with low manipulability and highlights that these designs are numerically sensitive and may develop the possibility of actuator saturation. For minimally invasive surgeries, such ill conditioning can increase tracking errors and jeopardize safety. Therefore, the singularity evaluation reaches an indubitable conclusion to perform geometric optimization of the HSR's parallel platform.

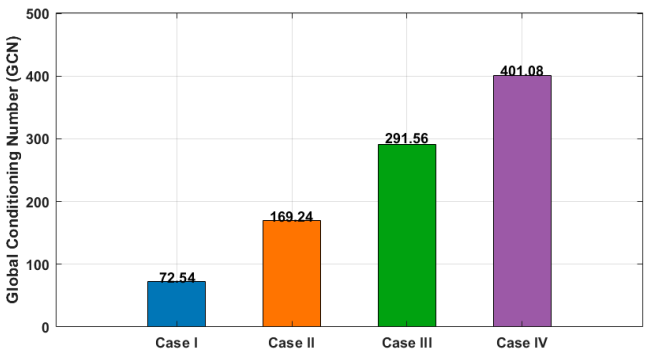


Figure 4. Values of the GCN for four test cases. **Case I**: Different joint angles and different upper and lower plate radii. **Case II**: Different joint angles and same upper and lower plate radii. **Case III**: Same joint angles and different upper and lower plate radii. **Case IV**: Same joint angles and same upper and lower plate radii.

Table 2. GCN values for four test cases of singularity analysis.

Cases	Upper Plate Joint Angle (°)	Lower Plate Joint Angle (°)	Upper Plate Radius (mm)	Lower Plate Radius (mm)	GCN
Case I	30	60	20	30	72.54
Case II	30	60	30	30	169.56
Case III	60	60	20	30	291.56
Case IV	60	60	30	30	401.08

4. Design Optimization

One of the major objectives of this study is to achieve a well-conditioned and precise hybrid surgical robot through design optimization of its parallel platform. But accomplishing this goal is difficult with higher values of GCN. Adjustments of geometrical, kinematic, and performance parameters are required in order to refine the workspace of the platform by reducing the singular configurations [46,47]. So far, we have assessed the performance of the platform on the basis of its condition number, but for performing the surgical tasks precisely, some other parameters also play a crucial role, which require analysis as well. Keeping this in mind, the design of the HSR's parallel platform has been optimized by considering three core parameters, i.e., GCN, actuator forces, and stiffness. The target is to achieve a trade-off between these three parameters by changing the geometric properties of the platform during the optimization process. An overview of these performance indices has been provided. Moreover, this section presents a single-objective optimization of the platform targeting reduction of its GCN mainly. In the next phase, multi-objective optimization is proposed and explained for obtaining a more efficient and versatile design of the HSR's platform. Finally, a workspace evaluation of the optimized design of the HSR's platform has been provided, which helps in understanding the improved performance of the platform as well as its enhanced range of motion.

4.1. Performance Indices

The parallel platform's design optimization targets three performance indices: GCN, actuator force, and stiffness, because together they represent the information about the system's kinematic dexterity, mechanical effort, and load-bearing capacity that are essential for safe and accurate surgical procedures. GCN is a measure of Jacobian conditioning that determines to what extent the actuator motions are optimally mapped into end effector motions and will therefore be a measure of the risk of singularities and susceptibility to input errors. Actuator forces obtained from the inverse of the Jacobian are the actual forces needed by the actuators to follow the trajectory or reject external wrenches. Stiffness, which is defined by the actuator stiffness matrix and Jacobian, controls the deviation of the platform under load and the resulting posture error.

These three metrics are tightly coupled as a high GCN indicates bad conditioning, and it will amplify errors, which in return usually require more force from the actuator to perform the same task, while a lack of stiffness allows these amplified forces to cause large deflections that will lead to the loss of even more accuracy and possibly change the effective Jacobian. Hence, neglecting any one of these indices during design therefore produces certain types of failure, such as ignoring GCN risking singularities and uncontrollable sensitivity; ignoring high actuator force use resulting in excessive use of energy, as well as wear and thermal or vibrational problems; and stiffness issues in the actuator system potentially causing unacceptable deflections and loss of positional accuracy, as well as unsafe interaction with tissue. Accordingly, the simultaneous optimization of all three indices must be realized in order to design a surgically robust and efficient parallel platform.

A detailed description of the condition number and GCN have already been provided previously, so this section will cover the other two performance indices, i.e., actuator force and stiffness.

4.1.1. Actuator Force

Actuators in parallel platforms generate forces that are required to execute the desired task. These forces bring about motion by effectively distributing the applied external wrench (forces and torques) across the whole platform's structure [48,49]. There exists a relation between these forces and an applied external wrench that is defined in terms of the Jacobian matrix. This relation is given in Equations (24) and (25).

$$F_a = J^{-1} \begin{bmatrix} F_P \\ M_P \end{bmatrix} \tag{24}$$

$$F_L = \text{norm}\left(J^{-1} \begin{bmatrix} F_P \\ M_P \end{bmatrix} \right) \tag{25}$$

where F_a is the platform's actuator force, J^{-1} is inverse of the Jacobian matrix, and $\begin{bmatrix} F_P \\ M_P \end{bmatrix}$ is the applied external wrench. Equation (25) gives the norm of actuator forces F_L, which is intended to be minimized.

As mentioned earlier, the external wrench is distributed equally among the six links of the platform; it is safe to assume that the platform is a rigid body, and it does not face any kind of deformation. Moreover, all the link forces associated with the platform must be linearly independent from each other, otherwise they will have an impact on the Jacobian matrix. The Jacobian matrix may become singular, and the HSR's platform may experience loss of degrees of freedom.

4.1.2. Stiffness

The stiffness of the HSR plays a crucial role in its motion and precision as it resists the external disturbances, refraining the system from undesired deflection and permanent damage. The overall stiffness of the HSR is highly dependent on the stiffness values of both of its components, mainly the parallel platform. In the parallel robotic platform, the stiffness value is dictated by three main factors, i.e., actuator configuration, distribution of forces throughout the platform's links, and the structural design of the platform. The relation between all these factors and the platform's stiffness is described by implementing linear small displacement assumptions that state that the parallel platform's displacements and rotations $\Delta p \in \mathbb{R}^6$ about a pose are so small that a first-order linear relation exists between them. The Jacobian matrix derived in the previous section helps to map a relation between the displacements and rotations of the platform $\Delta p = [\Delta x \Delta y \Delta z \Delta \psi \Delta \psi \Delta \varphi]^T$ and change in actuator lengths ΔL by Equation (26). The sign Δ denotes small changes in displacements, rotations, and actuator lengths.

$$\Delta L = J \Delta p \tag{26}$$

According to actuator force-displacement law:

$$\Delta F_a = K_a \Delta L \tag{27}$$

where $K_a = diag(k_{a1},\ k_{a2},\ \ldots, k_{a6})$ is the stiffness matrix of all six platform's actuators [50]. For determining Cartesian stiffness, the wrench (ΔM_P) equilibrium must exist in the system which is defined as:

$$\Delta M_P = J^T \Delta F_a \tag{28}$$

Substituting Equations (27) and (28) in Equation (29) results in Cartesian stiffness K_s.

$$\Delta M_P = J^T \Delta F_a = J^T K_a \Delta L = J^T K_a J \Delta p \tag{29}$$

Hence,

$$K_s = \frac{\partial M_P}{\partial L} = J^T K_a J \tag{30}$$

The platform's stiffness matrix K_s is a symmetrical matrix containing singular values Σ_i, which indicate stiffness in the corresponding principal axes. These singular values can be obtained by implementing the concept of singular value decomposition (SVD). The least singular value is the weakest stiffness of the platform. In order to enhance the precision and performance of the platform as well as the HSR, the diagonal of the minimum of these least singular values will be maximized in this optimization problem.

4.2. Single-Objective Optimization

The increase in efficiency of the 6-DOF parallel platform is directly proportional to minimizing the GCN values of its Jacobian matrix. This is accomplished by optimizing the design of the platform by changing its geometrical parameters. In this case, the design variables are the angles between the joints of both upper and lower plates ($\alpha_i,\ \beta_i$) and the radii of both plates ($r,\ R$), as described by variable X in Equation (31). Throughout the optimization process, these parameters were changed to observe their effect on the values of the GCN.

$$X = \{\alpha_i, \beta_i, r, R\} \qquad \text{where i} = 1, 2, \ldots, 6 \tag{31}$$

The design constraints for this optimization technique have been presented in Equations (32) and (33). Referring to Figure 2, the joint angles of both plates should be:

$$\left.\begin{array}{l} 0 \leq \beta_i \leq 60^{\circ} \\ 0 \leq \alpha_i \leq 30^{\circ} \end{array}\right\} \tag{32}$$

The radius of lower and upper plate should be:

$$\left.\begin{array}{l} 25 \text{ mm } \leq R \leq 55 \text{ mm} \\ 15 \text{ mm } \leq r \leq 35 \text{ mm} \end{array}\right\} \tag{33}$$

The aim of this optimization problem is to obtain a design for the HSR's parallel platform with the lowest value of GCN; this goal is defined by employing a single-objective function f_1. This objective function is the GCN computed over a set of discrete poses for all the designs of the parallel platform obtained by varying design variables described in Equation (31). The Jacobian matrix J and condition number $k(J_i)$ at each pose are determined. The values of condition number $k(J_i)$ govern the objective function f_1, and minimizing f_1 reduces the kinematic conditioning of the parallel platform. The calculation of single-objective function f_1 is explained by the following equations.

$$P = \{(p_0,\ R_{XYZ}(\phi, \theta, \psi)) \ :\ (\phi, \theta, \psi) \in \{-60^{\circ}, 0^{\circ}, +60^{\circ}\}\} \tag{34}$$

For each pose $O \in P$, $(p_0,\ R_{XYZ}(\phi, \theta, \psi))$ defines the position and orientation of the upper moving platform.

$$\textit{Minimize } f_1(\mathrm{x}) = \mathrm{GCN}(\mathrm{x}) = \frac{\sum_{i=1}^{n} k(\mathrm{J}(x, O_i))}{n} \tag{35}$$

where x is the parallel platform's candidate design, n is the number of discrete poses, and $k(\mathrm{J}(x, O_i))$ is the condition numbers of the platform computed for x design at a certain pose O_i. The technique employed for single-objective optimization is an evolutionary algorithm known as genetic algorithm (GA). The process began by initializing the optimization process by deciding the performance parameters for GA, provided in Table 3a. The next step was the calculation of the fitness function values followed by the selection of operator, crossover, and mutation among the populations and, finally, evaluation of the results. The operator selected in this case was rank-based selection, which helped in determining the best solution among the evolving generations of parents and offsprings. The optimization process was run for 200 iterations in order to have a good convergence of Pareto optimal solutions. The results of single-objective optimization are illustrated by Figure 5. The results depict a monotonic improvement in the objective function f_1, which began around the 55th generation and continued till the 200th generation, where the optimization process terminated upon meeting the convergence criteria. From the trend of the curve, it is evident that the GCN has been effectively reduced by improving the platform's design through optimization. An optimal value of 1.78 has been obtained. No doubt the GA demonstrated satisfactory results in terms of GCN evaluation, but the issues related to stiffness and actuator forces still persisted. The optimization results of this technique are summarized in Table 3b,c.

Table 3. (**a**) Performance parameters for GA-based single-objective optimization technique. (**b**) Optimized design variables (single-objective GA). (**c**) Results of optimized objective functions for optimized design based on GA optimization.

(**a**)	
Parameters	**Values**
Population size	300
Crossover probability	0.85
Mutation probability	0.01
Tolerance	10^{-6}.
(**b**)	
Design Variables X (Degrees, mm)	**Optimized Values (Degrees, mm)**
Upper plate angles (α_i)	25.3, 60.7, 87.2, 115.8, 143.4, 171.6
Upper plate radius (r)	29.66
Bottom plate angles (β_i)	41.8, 93.3, 151.9, 210.5, 269.1, 327.4
Bottom plate radius (R)	44.21
(**c**)	
Parameters	**Values**
GCN	1.78
Norm of actuator forces (N)	105
Stiffness (N/m)	542

The values of stiffness and norm of actuator force in this case are 542 N/m and 105 N. This occurred due to the fact that single-objective optimization focuses on refining the value of one objective at a time and may find it difficult to tackle multiple performance parameters at the same time. The requirement of design optimization is to attain a trade-off among all three parameters without compromising any of them. Hence, these simulations proved that it cannot be achieved through single-objective optimization, so the next goal is to simultaneously optimize all three parameters through multi-objective optimization.

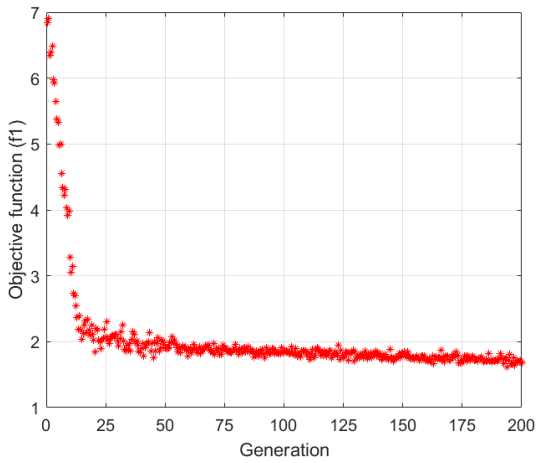


Figure 5. Single-objective GA convergence of the objective function f_1 versus the generation index. The solid curve depicts the best-so-far value of GCN.

4.3. Multi-Objective Optimization

Multi-objective optimization deals with the simultaneous optimization of two or more objectives without prioritizing any single one. In comparison with single-objective optimization, this technique generates a set of optimal solutions with no particular solution that is strictly better than the other one. Over the years, researchers have employed different multi-objective optimization techniques based on weighted sum methods and evolutionary algorithms. Among these, the non-dominated sorting genetic algorithm II (NSGA-II) has been used widely due to its benefits like quick non-dominating sorting, a crowding distance approach, and the concept of elitism [51]. This rapid non-dominating sorting assigns Pareto fronts to the solutions based on dominance criteria, and crowding distance is used to make these solutions diverse and unique from the previous ones. The concept of elitism enhances the convergence of optimal pareto fronts by preserving the best solutions among parents and offsprings. Figure 6 provides a detailed flowchart of how NSGA-II performs multi-objective optimization. Initially the generation counter (i) begins with a zero value and stops upon fulfilling the conditions of the dual termination criterion. The optimization algorithm terminates either when the solution converges and no considerable changes or improvements are observed over several generations or when the maximum number of generations is attained.

As the name suggests, evolutionary algorithms including NSGA-II mimic the phenomenon of natural selection. The initial set of solutions that evolves over the course of optimization process is known as population, whereas new solutions that are being generated from this population are termed as offsprings. The generation of both population and offsprings is dependent on key parameters known as crossover, selection, mutation, and crowding distance. The crossover is responsible for generating offspring from the initial population, selection criteria help in discarding incompetent solutions, mutation aids in evaluating optimal solutions, and crowding distance maintains diversity among generations while solving the optimization problem. Any optimization problem is defined by an objective function, which in the case of the HSR's platform is described by the following Equation (36).

$$\left.\begin{array}{c} Minimize\ f_1(\mathrm{x}) = \mathrm{GCN}\ (\mathrm{x}) = \frac{\sum_{i=1}^{n} k(\mathrm{J}(x,O_i))}{n} \\ Minimize\ f_2(\mathrm{x}) = F_L(x) = norm\left(J^{-1}\begin{bmatrix} F_{Px} \\ M_{Px} \end{bmatrix}\right) \\ Maximize\ f_3(\mathrm{x}) = K_s(x) = \mathrm{Min}(diag(\sum_{1\mathrm{x}}, \sum_{2\mathrm{x}}, \sum_{3\mathrm{x}}, \sum_{4\mathrm{x}}, \sum_{5\mathrm{x}}, \sum_{6\mathrm{x}})) \end{array}\right\} \quad (36)$$

In the above equation, x is the candidate design of the parallel platform, $f_1(\mathrm{x})$ is the first objective function, $f_2(\mathrm{x})$ is the second objective function, $F_L(x)$ is the norm of actuator forces for x design which is to be minimized, $\begin{bmatrix} F_{Px} \\ M_{Px} \end{bmatrix}$ denote wrench values for the platform's x design, $f_3(\mathrm{x})$ is the third objective function, $K_s(x)$ is the stiffness matrix of x design, and $\sum_{1x}, \ldots, \sum_{6x}$ are singular values for each actuated leg of the x design. The design variables and constraints for the NSGA-II optimization are the same as they were defined for the single-objective optimization presented by the set of Equations (32)–(35). The key parameters necessary to decide the course of the platform's optimization are listed in Table 4a.

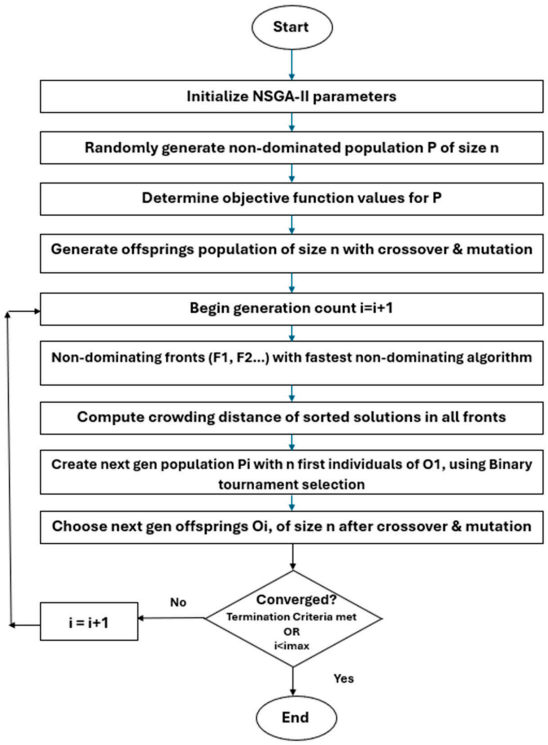


Figure 6. Flowchart of the NSGA-II algorithm with dual termination criterion: either convergence upon achieving termination criteria or reaching the maximum number of generations.

Table 4. (**a**) Performance parameters for NSGA-II-based multi-objective optimization technique. (**b**) Optimized design variables (multi-objective NSGA-II). (**c**) Results for the optimized objective functions for optimized design based on NSGA-II optimization.

(**a**)	
Parameters	**Values**
Population size	500
Crossover probability	0.8
Mutation probability	0.09
Mutation distribution index	15
Crossover distribution index	30
(**b**)	
Design Variables (Degrees, mm)	**Optimized Values (Degrees, mm)**
Upper plate angles (α_i)	6.7, 33.2, 61.8, 89.4, 117.6, 151.3
Upper plate radius (r)	23.52
Bottom plate angles (β_i)	5.8, 57.3, 115.9, 174.5, 233.1, 291.4
Bottom plate radius (r)	37.84

Table 4. *Cont.*

(c)	
Parameters	**Values**
GCN	2.21
Norm of actuator forces (N)	7.66
Stiffness (N/m)	1339

The results began to converge around 160 iterations, and at this stage it was determined that optimal solutions for the HSR's platform had been achieved. It should be kept in mind that NSGA-II-based multi-objective optimization algorithm yields a set of Pareto-optimal solutions instead of a single optimum solution, as presented in Figure 7. The goal of this approach is to find a representative set of the best trade-off solution, often termed as Pareto fronts, from which the user can choose the most suitable design based on their requirements. Referring to the Pareto fronts depicted in Figure 6, the final design model for the HSR's parallel platform was selected based on thorough observations and intuitions, ensuring a reasonable balance between all three objective function values. Minimizing the GCN along with other parameters was a major concern because it directly impacts the performance of those parameters as well as the dexterity of the whole system. Maximum values of GCN were recorded between 1 and 7, and the norm of actuator forces varied between 5 N and 25 N. The best trade-off observed between these two parameters was 2.36 and 7.55 N. In the graph depicting the optimal values of GCN plotted against the stiffness of the platform, the achievable value for GCN is around 2.12, and for stiffness, it is 1356 N/m. The trade-off values for the norm of actuator forces and stiffness were determined to be 8.28 N and 1274 N/m. Based on the observations and results of multi-objective optimization, the design variables and objective function values of the optimized model of the HSR's parallel platform are in Table 4b,c.

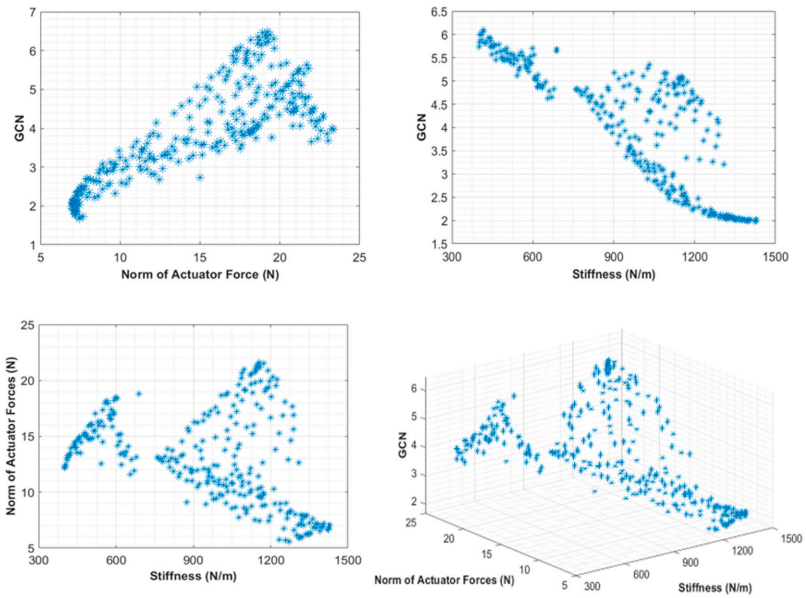


Figure 7. Pareto-optimal fronts obtained from NSGA-II-based multi-objective optimization. All these graphs present the trade-offs among objective function values of GCN, stiffness, and norm of actuator forces of the HSR's parallel manipulator.

4.4. Workspace Evaluation

Once the platform is optimized, the next step is its workspace analysis. Workspace analysis determines the feasible range of motion where the platform can perform the desired tasks with stability and precision without reaching singular configurations. Moreover,

surgical operations and procedures demand a highly reliable robot that can place the tool and perform the required task precisely. The manipulator's workspace determines the range of positions that can be achieved by the mechanism considering its geometric and structural constraints. In other words, the workspace also defines the space in which the inverse kinematics solutions of the manipulator exist without any singularity. Several approaches can be used for the evaluation of the manipulator's workspace, including analytical, numerical, and experimental methods [52]. Of these, numerical methods are commonly used since they can easily deal with complex geometries and constraints.

In this research work, a workspace evaluation algorithm of the HSR's parallel platform has been developed using MATLAB® based on the discretization method. This approach involves the knowledge of the inverse kinematics solutions of the platform when it moves radially along X and Y axes and vertically along the Z axis. The feasible poses of the platform are estimated iteratively within a predetermined subspace. This algorithm begins the iterative process by sub-dividing space through a hollowed cylindrical methodology, in which every point will be validated upon checking the inverse kinematic solutions. The values of Euler angles ϕ and θ are varied between a range of -60 degrees and 60 degrees with a step size of 0.2 for all iterations. The elevation limit for vertical motion in the Z axis was kept at 50 mm. The iterative process computes the pose values for different sets of Euler angles ϕ and θ and elevation in the Z axis. A validation process confirms all potential valid positions. The conditions of validation criteria are:

- **Leg length feasibility:** The solution is to be retained only if the parallel platform's actuator leg lengths satisfy the length constraint, i.e., $l_i \leq 45$ mm.
- **Joint limits:** The pose will be considered when the actuated legs' orientation relative to spherical joints is within the allowable limit of 60 degrees, keeping in view the limitations of spherical joints [53].
- **Collision avoidance:** Any pose leading to collisions between top and bottom plates of the parallel platform or excessive actuator crossing should be discarded.
- **Condition number evaluation:** Any pose with a singular Jacobian matrix or extremely high values of condition number should be excluded.

The last step is to view the platform's workspace by plotting the verified data points as depicted in Figure 8. This figure denotes the feasible workspace of the HSR's parallel platform. The process of iterative mapping makes the interpretation of the robot's kinematic ability clearer. Through the usage of this computational method, a complete description of the achievable workspace is obtained. The approach implemented is an efficient method of examining the reachability and dexterity of the parallel platform of the HSR.

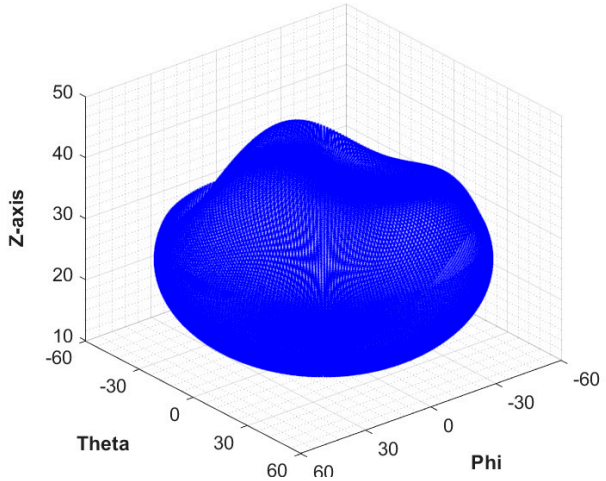


Figure 8. Workspace of the optimized HSR design.

5. Motion Planning

After designing a surgical robot and developing its kinematic and geometric models, the next step is to test its motion planning ability for any surgical procedure. Motion planning refers to a process of assessing the performance and precision of a surgical robot for a predefined trajectory. This trajectory is a connection of different pose values defined in the Cartesian or joint space of the robot. The robot plans the motion by utilizing its inverse kinematic model and determines the required leg/link lengths to reach that pose. In this case, for assessing the motion planning abilities of the HSR, two different trajectories have been chosen consisting of multiple pose points in Cartesian space. These pose points are the spatial configurations and orientations that connect and form the surgical procedure trajectory.

5.1. Trajectory 01: Point-to-Point Path Tracing

The first trajectory consisted of a ten-point Cartesian motion sequence aimed at investigating the capability of the robot to execute precise incremental positioning as is usually needed during sensitive tissue approaches, instrument alignment, or even micro-adjustment maneuvers for minimally invasive procedures. The path depicted in Figure 9 shows two controlled variations along the x, y, and z axes, passing through intermediate positions instead of a linear sweep. This reflects realistic surgical motions where the tool to be moved is required to move from one anatomical location to the next or approach an operative region by small increments. The distances define a uniform spacing between trajectory points, and the path geometry is well within the platform's dexterous workspace to avoid unnecessary strain of the actuators as well as the risk of singular configurations arising from the workspace boundary.

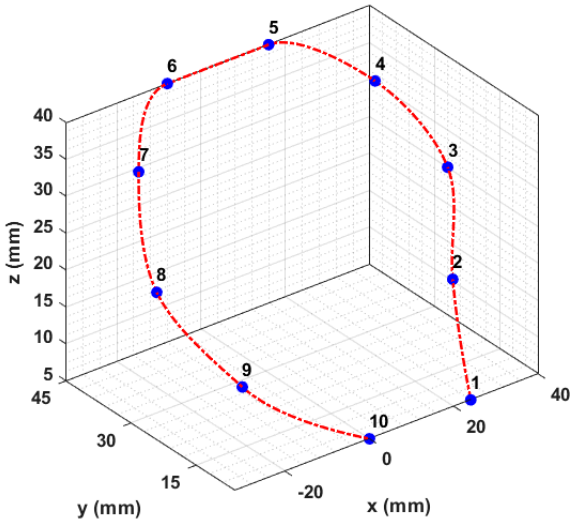


Figure 9. Desired Trajectory 01: point-to-point path movement.

The optimized model of the HSR's parallel platform tracked the desired trajectory quite efficiently, which can be observed by the results recorded in Table 5a and Figure 10. The average positional error between the desired and executed end effector trajectory was around 0.07 mm, with the maximum error being less than 0.12 mm. These values are much less than the 0.5 mm tolerance, which is generally suggested for neurosurgical and microsurgical robotic interventions, showing that the system is able to reproduce a path with high precision without measurable drift and cumulative error accumulation.

Table 5. (**a**) Desired Trajectory 01: point-to-point path movement defined in terms of Cartesian space. (**b**) Dynamic response parameters of the HSR's optimized platform for tracking Trajectory 01: point-to-point path movement.

(**a**)

Pose	X-Coordinate (mm)	Y-Coordinate (mm)	Z-Coordinate (mm)
1	26	7	5
2	26	7	15
3	39.81	20.2256	25.301
4	25.389	32.692	35.605
5	21.2701	44.947	40
6	−8	45	40
7	−19.3891	37	35.605
8	−30	25	25
9	−10.772	27.797	15
10	0	6	5

(**b**)

Parameters	Values	Units
Time	10	s
Mean position error	0.07	mm
Peak position error	0.12	mm
Mean velocity	4.8	mm/s
Peak velocity	8.45	mm/s
Mean acceleration	2.31	mm/s^2
Peak acceleration	5.87	mm/s^2
Mean jerk	8.92	mm/s^3
Peak jerk	18.4	mm/s^3
Maximum torque	0.5	Nm

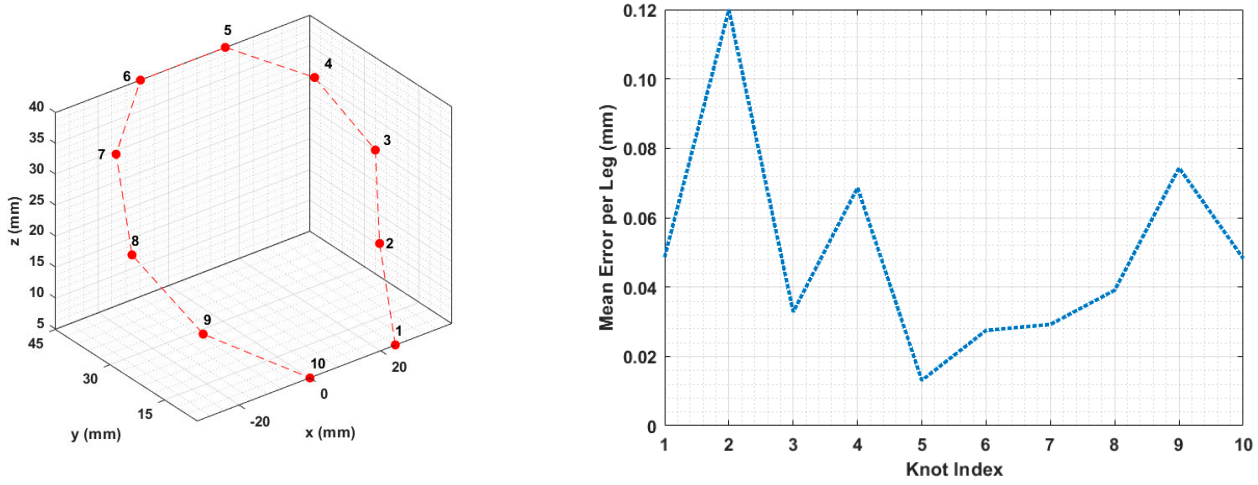


Figure 10. (**Left**): Traced Trajectory 01: point-to-point path movement by the HSR's optimized parallel platform; (**Right**): mean position error differentiating between desired and traced Trajectory 01.

Kinematic behavior of the parallel platform is clearly smooth according to the dynamic motion analysis performed during the motion planning of this trajectory. The mean leg velocity during motion was about 4.8 mm/s; the maximum velocity of 8.45 mm/s indicates that the motion was well paced and not subject to fast-paced fluctuations. Acceleration was low with the mean set as approximately 2.31 mm/s^2 and the maximum as approximately 5.87 mm/s^2, verifying that the motion profile does not have sharp dynamic loads. The

jerk, which is an important smoothness and system vibration indicator, remained very low, with mean jerk being around 8.92 mm/s^3 and peak jerk around 18.4 mm/s^3. These low jerk levels are very important in surgical applications because they ensure the reduction of tool vibration, overshoot of actuator forces, and soft tissue manipulation. All six actuator torques remained under moderate range, not exceeding 0.5 Nm, indicating no actuator was overloaded during the motion planning procedure. The minute error values of actuator leg lengths also support the claim that the HSR's parallel platform can be used for surgical procedures where point-to-point movement is required. All the results of dynamic motion analysis are summarized in Table 5b and depicted in Figure 11.

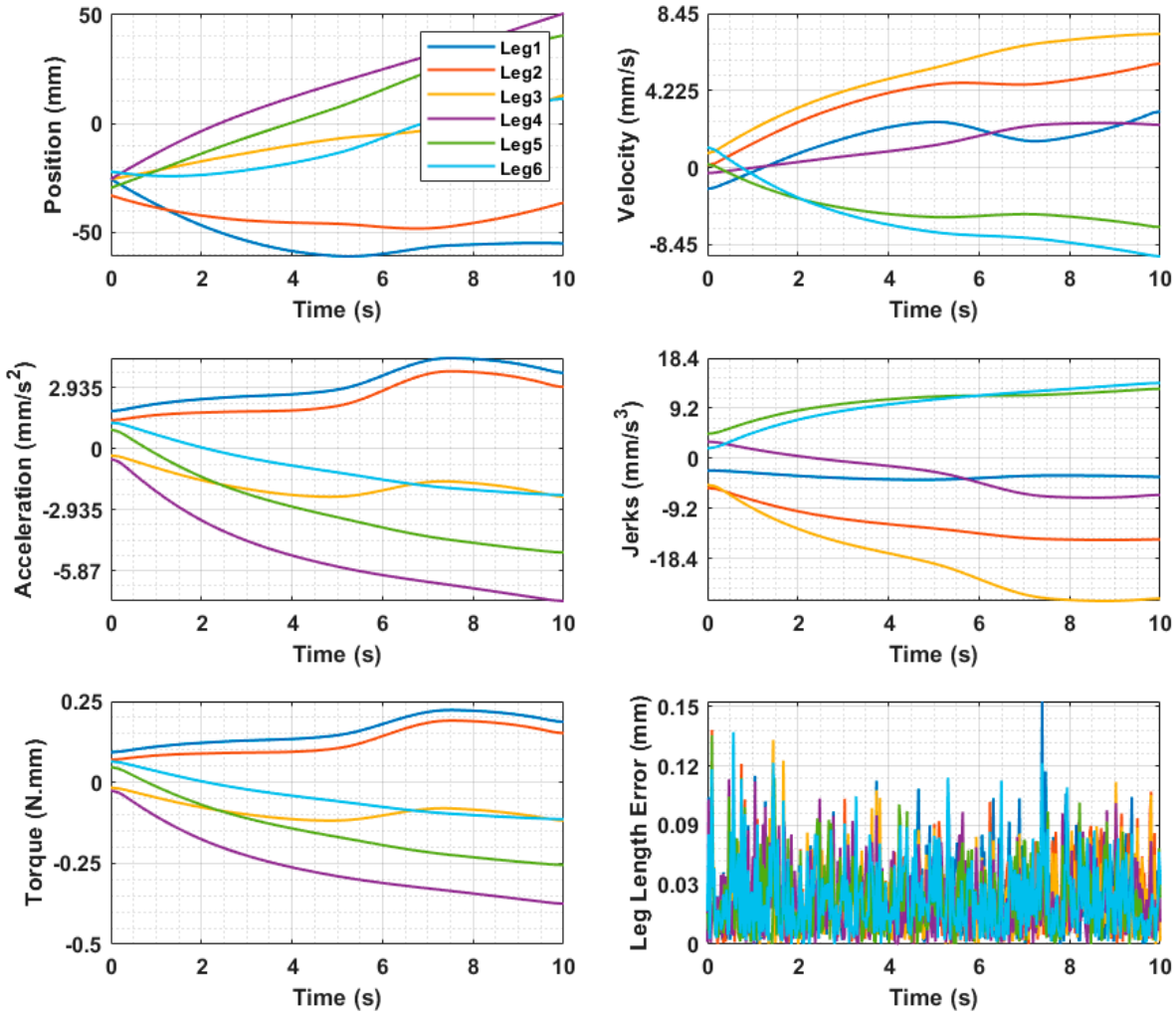


Figure 11. Dynamic responses of the HSR's optimized parallel platform demonstrated while tracking Trajectory 01: point-to-point path movement.

5.2. Trajectory 02: Spatial Spiral Trajectory

The second trajectory selected for assessing the motion planning capabilities of the HSR's parallel platform is a three-dimensional helical or spiral motion, and it is a more complicated toolpath that requires simultaneous coordinated changes in all the Cartesian axes. This kind of trajectory is typical of surgical movements like tracing the lesion boundaries, electrode placement sweeps, or curved approach movements. The Cartesian coordinates follow a circular pattern in the x–y plane and increase monotonically in z, as is visible in Figure 12, and therefore, the platform needs to maintain coordinated control in the actuators throughout the motion.

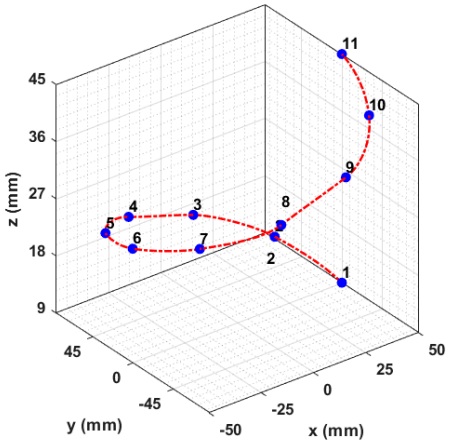


Figure 12. Desired Trajectory 02: Spatial spiral trajectory.

Table 6a and Figure 13 demonstrate how well the HSR's platform traced this spiral trajectory. The traced trajectory is close to the desired path; however, slight deviations start to occur due to the increased kinematic coupling for maintaining the spiral path. Despite the complexity of the desired trajectory, the optimized platform managed to deliver the required motion with a mean error of around 0.17 mm and peak position error not higher than 0.375 mm. The average position error is less than 0.5 mm, which is still below commonly assumed surgical tolerance limits. This level of accuracy validates the effectiveness of the controller and mechanical design, even when the movement is dynamic and continuous path movement, and not just in slower point-to-point positioning.

Table 6. (**a**) Desired Trajectory 02: spatial spiral trajectory, defined in terms of Cartesian space. (**b**) Dynamic response parameters of the HSR's optimized platform for tracking Trajectory 02: spatial spiral trajectory.

(**a**)

Pose	X-Coordinate (mm)	Y-Coordinate (mm)	Z-Coordinate (mm)
1	50	0	9
2	30.27	26.777	16.441
3	10.9017	42.1057	17
4	−8.993	43.0993	20.922
5	−24.2345	45.7785	22
6	−50	1.224	27
7	−34.9017	−46.7782	29
8	−19.9027	−48.1057	35
9	35.8713	−42.231	38
10	37.8213	−31.775	42
11	50	−2.449	45

(**b**)

Parameters	Values	Units
Time	10	s
Mean position error	0.17	mm
Peak position error	0.375	mm
Mean velocity	7.43	mm/s
Peak velocity	11.28	mm/s
Mean acceleration	3.86	mm/s^2
Peak acceleration	7.92	mm/s^2
Mean jerk	11.34	mm/s^3
Peak jerk	21.6	mm/s^3
Maximum torque	1.2	Nm

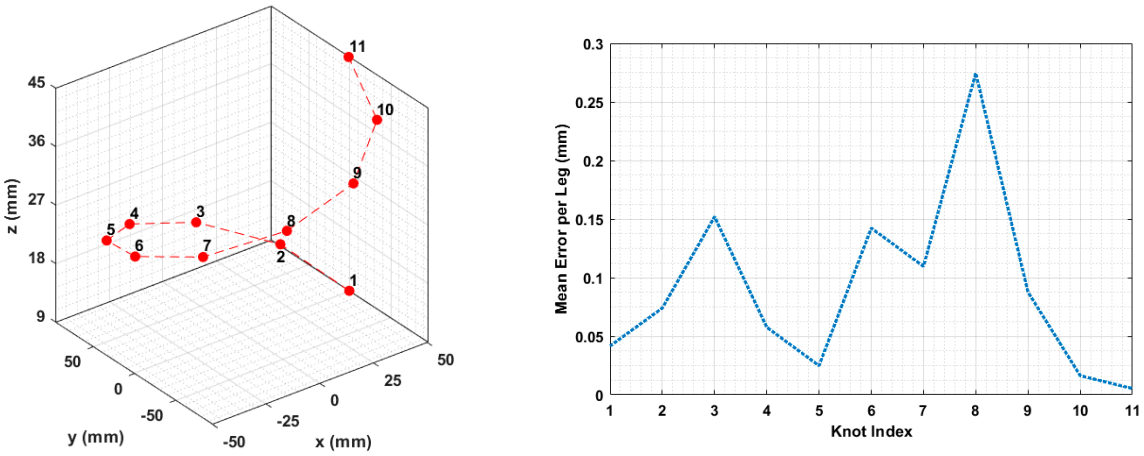


Figure 13. (**Left**): Traced Trajectory 02: spatial spiral trajectory by the HSR's optimized parallel platform; (**Right**): mean position error differentiating between desired and traced Trajectory 02.

Complexity of motion resulted in higher dynamic response levels that were proportional to the motion complexity. Results of dynamic analysis of the platform for Trajectory 02 have been added in Table 6b and Figure 14. The mean actuator velocity increased to 7.43 mm/s, with a peak value of 11.28 mm/s, which is consistent with the longer and curved stroke. The mean acceleration increased to 3.86 mm/s^2 with a peak near 7.92 mm/s^2, which is again under the normal range and does not cause abrupt or sudden changes in the motion of the platform. Jerk values were kept within clear limits, i.e., 26.1 mm/s^3, which indicate the complexity of the trajectory and the efforts delivered by the platform's actuators for providing smooth transitions and avoiding unnecessary oscillations in the results. While there was an increase in the actuator torque to 1.2 Nm, no discontinuities were present, suggesting that load distribution and good actuator coordination was maintained throughout the spatial sweep. The successful motion planning of both trajectories backs the claim that the optimized model of the HSR's parallel platform is suitable for delicate surgical interventions.

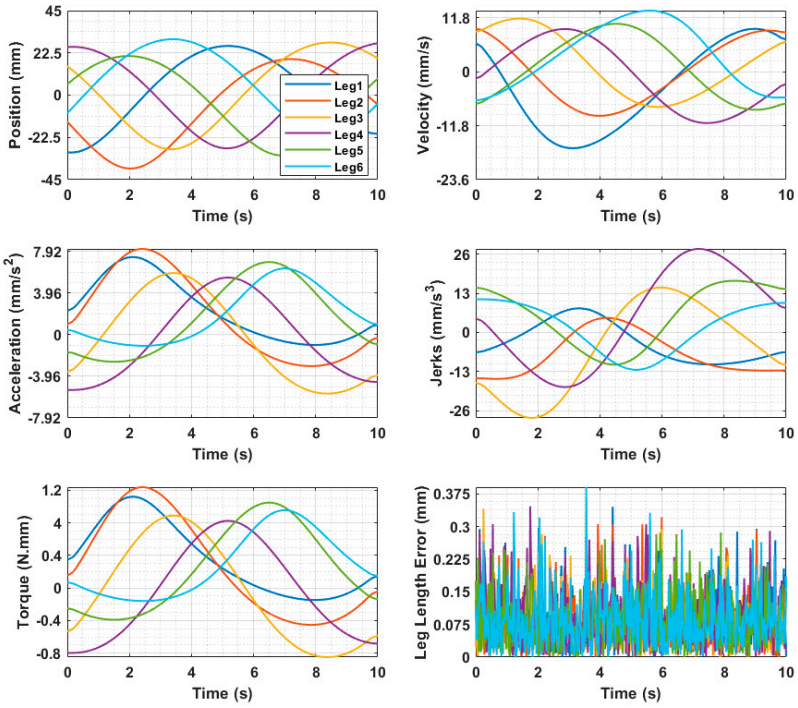


Figure 14. Dynamic responses of the HSR's optimized parallel platform demonstrated while tracking Traced Trajectory 02: spatial spiral trajectory.

6. Discussion

An 8-DOF design of the HSR has been proposed in this study, which faced a restricted range of motion due to inherent limitations of its parallel platform. To address this issue, a multi-stage design analysis of the platform has been implemented in this research. This analysis covered three different kinds of models and analyses, which helped in identifying the restrictions and constraints of the platform's design. The multi-stage analysis highlighted serious issues in the HSR's parallel platform's initial model and raised the need for optimization of its design based on its geometric and structural parameters. The optimized model was tested for its motion planning capabilities as described in Section 5. This section provides a detailed discussion on each section of this paper.

6.1. Design Analysis

The first analysis, named kinematic analysis, determined the leg lengths that are required to reach the desired surgical pose. Any deviation in these values may lead to positional inaccuracies and errors in the platform's performance. The second analysis, termed as geometrical analysis, employed the information from the findings of kinematic analysis and derived a relation for the Jacobian matrix, which not only influences the angular velocity and wrench values of the platform but also plays a huge role in estimating its condition number. The third analysis is singularity analysis, which is governed by the values of the GCN. It involved four test cases obtained by altering the geometric parameters of the platform like joint angles of the upper and lower plates and the radii of both plates. The values of the GCN were recorded when each test case explored 150 different poses based on Latin hypercube sampling (LHS). The results of this analysis, tabulated in Table 2, indicated higher values of GCN, indicating clear deterioration of the platform's kinematic conditioning when the design of the platform was more symmetrical. These high GCN values strongly justify the need for the parallel platform's design optimization in order to improve its performance and maneuverability.

6.2. Comparison of Design Optimization Techniques

This study uses both GA and NSGA-II to optimize the parallel platform of an 8-DOF HSR in order to provide an obvious comparative frame with optimization methodologies that were reported in the existing literature. The pattern search approach given in [26] is a deterministic derivative-free technique designed to maximize a single global performance index (GPI). While it is efficient for single-objective problems, it cannot account for trade-offs between several performance parameters such as dexterity, stiffness, and effort required by the actuator, and it is prone to converge at local optima. In contrast, the neural network-based optimization reported in [31] is based on a different paradigm, where the configurations of Stewart platforms are predicted for given tool orientations. Though successful for operational adaptation, this approach is limited to motion-level optimization, does not include structural design, and relies heavily on training data, hence limiting their generalizability and robustness.

On the other hand, the present research tests the exploratory capabilities of GA as well as NSGA-II for design-oriented optimization of the HSR's parallel platform. GA provides a powerful global search mechanism, which can efficiently search the complex, multimodal design spaces and find near-optimal solutions for a single objective such as GCN improvement. NSGA-II extends this ability by simultaneously optimizing a number of conflicting objectives like dexterity, stiffness, and actuator forces, employing Pareto dominance to maintain a balance between all the objectives. This evolutionary algorithm supports thorough exploration and efficient convergence, providing a resultant design that shows significant improvements in GCN, stiffness, and actuator forces.

In this research, the design optimization of the parallel platform began with the identification of parameters that influence its performance greatly. The deterioration of performance due to the major concern of the higher values of GCN was first attempted to be resolved through GA-based single-objective optimization. This approach significantly reduced the GCN to 1.78 but could not address the issues related to actuator forces and stiffness. The value of norm of actuator forces was high and the stiffness was low for a miniaturized model of the HSR's platform, as reported in Table 3c. The purpose of optimizing the design is to obtain a model with an optimal set of all three parameters without compromising any of them. This led to an evolutionary algorithm-based multi-objective optimization approach named NSGA-II. The attributes of this approach like non-dominating sorting, crowding distance, and the concept of elitism introduced faster convergence of results, diversity in the designs, and preservation of the best solutions among each generation. A comparison based on the performance parameters of both GA and NSGA-II is summarized in Table 7.

Table 7. Comparison between GA and NSGA-II based on significance for optimization of the HSR's parallel platform.

Parameter	GA	NSGA-II	Significance for Optimization
Population size	300	500	Larger populations introduce global search coverage and variety but extend computation time. The selected sizes provided appropriate exploration on a reasonable timescale.
Crossover probability	0.85	0.8	High crossover rates ensure exploitation by comparing the better individuals. Lower probability in NSGA-II ensures diversity across Pareto fronts without compromising convergence.
Mutation probability	0.01	0.09	Higher mutation in NSGA-II enables randomness and diversity across multiple objectives while avoiding premature convergence of results.
Crossover distribution index	–	30	It enables NSGA-II to preserve variety in multiple objectives by controlling the offspring spread.
Mutation distribution index	–	15	Identifies the amount of perturbation. The parameter of 15 is a middle ground between exploration and convergence.
Iterations	200	160	More iterations were required for GA, while the elitism and crowding distance were found to be more conducive to convergence efficiency in NSGA-II.
Runtime (s)	~2810	~2538	Despite a larger population and multiple objectives, NSGA-II converged faster.

A convergence in the results for NSGA-II was noticed around 160 iterations, and it was deduced that the optimal solution of the HSR's parallel platform has been achieved. The optimization process was also monitored in terms of computational time. The convergence of results at 160 iterations was obtained in 2538 sec with acceptable computational overhead on a 10th generation Intel(R) Core (TM) i5. The results reported in Tables 4a and 5b present the optimized design of the parallel platform, which has a GCN value of 2.21, minimized norm of actuator forces of 7.66 N, and maximized stiffness value of 1339 N/m. From Figure 7, the values of different Pareto-optimal fronts can be deduced based on the user's observations and requirements, and the highest values of each parameter can also be determined. The highest values of the GCN, norm of actuator forces, and stiffness are determined to be 6.53, 23 N, and 1475 N/m, respectively. An optimized design offering a good trade-off among performance parameters was selected, with GCN values closer

to unity so that the platform tracks and plans the desired trajectories without reaching the singular configurations. Furthermore, these close to unity values of the GCN also have an impact on the feasible range of workspace in which the platform operates, which is determined and depicted in Figure 8. Other than the reduction of the GCN, another milestone achieved by multi-objective optimization is the maximization of the minimal stiffness values in the workspace of the platform. At singular configurations, the platform not only lost its DOFs but also faced the loss of mechanical stiffness. This issue was catered for by improvement in GCN values, which led to enhanced stiffness within the platform's workspace. In comparison with GA, the optimized model of NSGA-II had 24 percent more value for the GCN; this is because GA focused on reducing GCN only, which led to overfitting for dexterity at the expense of mechanical robustness, while the goal of NSGA-II was to obtain the best trade-off among all three objectives being considered. Quantitatively, the NSGA-II-based optimization resulted in an approximately 147 percent improvement in stiffness and reduced actuator forces by about 93 percent with respect to the GA design while ensuring an acceptable dexterity. Reduction of the norm of actuator forced was an aim in this optimization, keeping in view the drawbacks of excessive forces that may cause accidental overshoots and tremors, wear and tear of the robot, and thermal buildup in the components. To avoid these issues and make it efficient for soft-tissue interactions, the actuator forces were minimized. After the optimization, the feasible workspace of the platform was analyzed, considering the joints, actuators, and other geometric constraints of the HSR's parallel platform.

In order to analyze the numerical strength and accuracy of the optimization results of the NSGA-II (Figure 6), a small-scale analysis of errors was conducted. Pareto-optimal convergence of the five independent optimization runs with the same parameter settings was reviewed. It was found that the standard deviation of the objective at convergence was similar and equal to ± 2.3, ± 3.1, and ± 2.7 percent in GCN, actuator force, and stiffness, respectively, with high precision in the results of the optimization process. The small variations are caused by the stochastic behavior of the crossover and mutation operations, without which the evolutionary algorithms bring random diversity. The fact that there is low dispersion among the runs is confirmation that the algorithm is consistent in converging to the same Pareto front as opposed to local minima that are random. The difference in the solutions does significantly influence engineering values and makes negligible differences in the qualitative trade-offs between objectives. This type of stochastic consistency analysis is consistent with existing methods of uncertainty assessment of multi-objective evolutionary algorithms [54].

6.3. Workspace of HSR

The workspace assessment in Section 4 revealed that the optimized design of the parallel platform of the 8-DOF HSR possesses a large and dexterous workspace and can continue to remain mechanically stable and singularity-free. The numerical discretization method enabled accurate mapping of feasible poses and a smooth and continuous workspace with no discontinuities, and this confirms the structural symmetry obtained after optimization. The optimized geometric parameters, especially plate radii and joint orientations, were improved as opposed to pre-optimized settings and offered better reachability in all translational and rotational directions. Workspace evaluation helped in avoiding the singular and collision-prone areas and determining a kinetically stable structure of the platform, resulting in a confined yet practically adequate workspace that could be utilized in surgery. This platform's workspace is, therefore, an optimized trade-off between optimized conditioning and stiffness, which validates that the NSGA-II optimized design has achieved

the improvement of motion performance of the HSR without compromising control of its parallel platform.

6.4. Motion Planning of HSR

The motion planning assessment in this study shows that the proposed hybrid surgical robot is able to realize both discrete and continuous motion patterns with excessive spatial precision and stable dynamic response. In the case of Trajectory 01, the robot had an average tracking error around 0.07 mm, with a peak deviation smaller than 0.12 mm, which shows that the HSR's platform has a good ability to reproduce the trajectory of waypoint-based movement. The resulting trajectory velocity and acceleration profiles did not exhibit overshoot and sharp transitions, and the magnitudes of jerk were low, which verified the undesired oscillation-free motion ability of the system for delicate situations in surgery. These characteristics indicate that the optimized parallel platform is appropriate for applications that require a fine positioning and controlled approach maneuver such as needle insertion, target alignment, or reorientation of the tool in close proximity to sensitive anatomic structures.

In the case of the 3D spiral path, where all three spatial axes would need to be coordinated, the optimized parallel platform performed a stable and accurate path, following with an average error of about 0.17 mm and a maximum error limited to 0.375 mm, which is within clinically acceptable limits of a minimally invasive procedure. Despite the increased curvature and dynamic coupling requirements, the velocity, acceleration, and torque curves were controlled; the jerk response was constrained, which showed continuous smooth motion; and mechanical oscillations were not induced. This demonstration confirms the fact that not only is the system capable of dealing with correct point-to-point positioning, but it can also assist in more complex, continuous navigation operations like contour tracking, surface following, or controlled tool sweeping when performing surgery. All these findings affirm that the HSR has the accuracy, stability, and dynamic fluidity to operate safely and accurately in any surgical operation and support its use in neurosurgical and other small-scale operating scenarios where motion accuracy is paramount.

7. Conclusions

The goal of this research was to provide a comprehensive framework of the design and optimization of an HSR that overcomes the limitations of constricted motion of parallel surgical manipulators. For achieving this goal, a complete design of the HSR was proposed in this study. The HSR's parallel platform faced constraints due to its limited workspace, so it was established that optimizing the design of the HSR based on the results of design analysis will significantly impact the performance of the HSR. A multi-stage analysis was conducted for this purpose. After developing the inverse kinematic model and geometric model of the parallel platform, its singularity analysis was conducted on the basis of its GCN. The results of this analysis indicated the need for an optimized model that would improve the platform's workspace. Initially, the platform was optimized using a GA-based optimization model focused on minimizing the GCN only. But this optimization improved the GCN only while compromising other important parameters like stiffness and actuator forces. In order to obtain a better trade-off among these three crucial performance parameters, NSGA-II-based multi-objective optimization was performed. An optimized design for the HSR was obtained using this approach, which was further analyzed on the basis of workspace analysis and motion planning of a 3D trajectory.

For further improvements in the design and optimization of the HSR, future studies can explore different optimization techniques to see the changes and variations in the optimized models of these techniques. Moreover, a comparison can be drawn indicating which

technique has been the most successful in optimizing the design of the HSR. Physical prototype development would significantly help in determining the strengths and weaknesses of the currently proposed design. The HSR couples the parallel mechanism and robotic arm like a serial manipulator to reach deep and difficult anatomical sites during surgical procedures. But such structural assembly may also create small vibrations at the serial connections because of dynamic forces transmitted through the parallel platform, and this may have a slight influence on the positioning accuracy when performing high-precision surgery [55] (add ref Modular). Thus, isolation and vibration control is very significant in the stability of robotic systems that are hybrid, which will be implemented in future studies. Depending upon the practical results, the design of the HSR can be improved further. Integration of advanced technologies like adaptive and intelligent controllers, automatic tool change, voice control, gesture control, haptic feedback mechanisms, etc., can considerably improve the user's experience and will aid in reducing the surgeon's fatigue and efforts during extensive surgical procedures.

Author Contributions: Conceptualization, A.K. and M.F.S.; methodology, A.K., M.F.S. and Z.K.; software, A.K.; validation, A.K., M.F.S. and M.U.F.; formal analysis, M.U.F.; investigation, A.K.; resources, F.K.D.; data curation, F.K.D. and S.Z.H.; writing—original draft preparation, A.K. and M.F.S.; writing—review and editing, Z.K., M.U.F. and S.Z.H.; visualization, A.K. and F.K.D.; supervision, M.U.F.; project administration, Z.K. and M.U.F.; funding acquisition, M.F.S. and F.K.D. All authors have read and agreed to the published version of the manuscript.

Funding: This research received no funding.

Data Availability Statement: The original contributions presented in this study are included in the article. Further inquiries can be directed to the corresponding author(s).

Conflicts of Interest: The authors declare no conflicts of interest.

Abbreviations

The following abbreviations are used in this manuscript:

HSR	Hybrid surgical robot
DOF	Degree of freedom
GCN	Global conditioning number
MATLAB	Matrix laboratory
3D	Three-dimensional
PP	Parallel platform
SM	Serial manipulator

References

1. Gawande, A. Two Hundred Years of Surgery. *N. Engl. J. Med.* **2012**, *366*, 1716–1723. [CrossRef]
2. Suh, J.H.; Kotecha, R.; Chao, S.T.; Ahluwalia, M.S.; Sahgal, A.; Chang, E.L. Current Approaches to the Management of Brain Metastases. *Nat. Rev. Clin. Oncol.* **2020**, *17*, 279–299. [CrossRef]
3. Liu, Y.; Wu, X.; Sang, Y.; Zhao, C.; Wang, Y.; Shi, B.; Fan, Y. Evolution of Surgical Robot Systems Enhanced by Artificial Intelligence: A Review. *Adv. Intell. Syst.* **2024**, *6*, 2300268. [CrossRef]
4. Antonov, A. Parallel–Serial Robotic Manipulators: A Review of Architectures, Applications, and Methods of Design and Analysis. *Machines* **2024**, *12*, 811. [CrossRef]
5. Pisla, D.; Plitea, N.; Gherman, B.G.; Vaida, C.; Pisla, A.; Suciu, M. Kinematics and Design of a 5-DOF Parallel Robot Used in Minimally Invasive Surgery. In *Advances in Robot Kinematics: Motion in Man and Machine*; Springer: Berlin/Heidelberg, Germany, 2010; pp. 99–106. [CrossRef]
6. D'Ettorre, C.; Mariani, A.; Stilli, A.; Baena, F.R.Y.; Valdastri, P.; Deguet, A.; Kazanzides, P.; Taylor, R.H.; Fischer, G.S.; DiMaio, S.P.; et al. Accelerating Surgical Robotics Research: A Review of 10 Years with the Da Vinci Research Kit. *IEEE Robot. Autom. Mag.* **2021**, *28*, 56–78. [CrossRef]

7. Maddahi, Y.; Zareinia, K.; Sepehri, N.; Sutherland, G. Surgical Tool Motion during Conventional Freehand and Robot-Assisted Microsurgery Conducted Using NeuroArm. *Adv. Robot.* **2016**, *30*, 621–633. [CrossRef]
8. Spinelli, A.; David, G.; Gidaro, S.; Carvello, M.; Sacchi, M.; Montorsi, M.; Montroni, I. First Experience in Colorectal Surgery with a New Robotic Platform with Haptic Feedback. *Color. Dis.* **2018**, *20*, 228–235. [CrossRef]
9. Seibold, U.; Kübler, B.; Bahls, T.; Haslinger, R.; Steidle, F. The DLR *Mirosurge* surgical robotic demonstrator. In *The Encyclopedia of Medical Robotics*; World Scientific: Singapore, 2018; pp. 111–142. [CrossRef]
10. Li, Y.; Hannaford, B.; Rosen, J. The Raven Open Surgical Robotic Platforms: A Review and Prospect. *Acta Polytech. Hungarica* **2019**, *16*, 9–27.
11. Thomas, B.C.; Slack, M.; Hussain, M.; Barber, N.; Pradhan, A.; Dinneen, E.; Stewart, G.D. Preclinical Evaluation of the Versius Surgical System, a New Robot-Assisted Surgical Device for Use in Minimal Access Renal and Prostate Surgery. *Eur. Urol. Focus* **2021**, *7*, 444–452. [CrossRef]
12. Kazanzides, P.; Zuhars, J.; Mittelstadt, B.; Williamson, B.; Cain, P.; Smith, F.; Rose, L.; Musits, B. Architecture of a Surgical Robot. In Proceedings of the IEEE International Conference on Systems, Man and Cybernetics, Chicago, IL, USA, 18–21 October 1992; Volume 2, pp. 1624–1629. [CrossRef]
13. Pisla, D.; Plitea, N.; Gherman, B.; Pisla, A.; Vaida, C. Kinematical Analysis and Design of a New Surgical Parallel Robot. In *Computational Kinematics*; Springer: Berlin/Heidelberg, Germany, 2009; pp. 273–282. [CrossRef]
14. Seide, K.; Faschingbauer, M.; Wenzl, M.E.; Weinrich, N.; Juergens, C. A Hexapod Robot External Fixator for Computer Assisted Fracture Reduction and Deformity Correction. *Int. J. Med. Robot.* **2004**, *1*, 64–69. [CrossRef]
15. Wolf, A.; Jaramaz, B.; Lisien, B.; DiGioia, A. MBARS: Mini Bone-Attached Robotic System for Joint Arthroplasty. *Int. J. Med. Robot. Comput. Assist. Surg.* **2005**, *1*, 101–121. [CrossRef]
16. Kobler, J.P.; Kotlarski, J.; Öltjen, J.; Baron, S.; Ortmaier, T. Design and Analysis of a Head-Mounted Parallel Kinematic Device for Skull Surgery. *Int. J. Comput. Assist. Radiol. Surg.* **2012**, *7*, 137–149. [CrossRef] [PubMed]
17. Wei, W.; Goldman, R.; Simaan, N.; Fine, H.; Chang, S. Design and Theoretical Evaluation of Micro-Surgical Manipulators for Orbital Manipulation and Intraocular Dexterity. In Proceedings of the 2007 IEEE International Conference on Robotics and Automation, Rome, Italy, 10–14 April 2007; pp. 3389–3395. [CrossRef]
18. Shoham, M.; Burman, M.; Zehavi, E.; Joskowicz, L.; Batkilin, E.; Kunicher, Y. Bone-Mounted Miniature Robot for Surgical Procedures: Concept and Clinical Applications. *IEEE Trans. Robot. Autom.* **2003**, *19*, 893–901. [CrossRef]
19. Nzue, R.M.A.; Brethé, J.F.; Vasselin, E.; Lefebvre, D. Comparison of Serial and Parallel Robot Repeatability Based on Different Performance Criteria. *Mech. Mach. Theory* **2013**, *61*, 136–155. [CrossRef]
20. Laribi, M.A.; Arsicault, M.; Riviere, T.; Zeghloul, S. Toward New Minimally Invasive Surgical Robotic System. In Proceedings of the 2012 IEEE International Conference on Industrial Technology, Athens, Greece, 19–21 March 2012; pp. 504–509. [CrossRef]
21. Kuo, C.; Dai, J.S. International Symposium on History of Machines and Mechanisms. In *History of Mechanism and Machine Science*; Springer: Berlin/Heidelberg, Germany, 2009; pp. 337–338. [CrossRef]
22. Pisla, D.; Gherman, B.G.; Suciu, M.; Vaida, C.; Lese, D.; Sabou, C.; Plitea, N. On the Dynamics of a 5 DOF Parallel Hybrid Robot Used in Minimally Invasive Surgery. In *Mechanisms and Machine Science*; Springer: Berlin/Heidelberg, Germany, 2010; Volume 5, pp. 691–699. [CrossRef]
23. Pisla, D.; Szilaghyi, A.; Vaida, C.; Plitea, N. Kinematics and Workspace Modeling of a New Hybrid Robot Used in Minimally Invasive Surgery. *Robot. Comput. Integr. Manuf.* **2013**, *29*, 463–474. [CrossRef]
24. Tanev, T.K.; Cammarata, A.; Marano, D.; Sinatra, R. Elastostatic Model of a New Hybrid Minimally-Invasive-Surgery Robot. In Proceedings of the 14th IFToMM World Congress, Taipei, Taiwan, 25–30 October 2015. [CrossRef]
25. Peng, Y.; Yu, H.; Du, Z. Design and Kinematic Analysis of a Hybrid Manipulator for Spine Surgery. In Proceedings of the 2016 IEEE International Conference on Mechatronics and Automation, Harbin, China, 7–10 August 2016; pp. 884–889. [CrossRef]
26. Liu, Q.; Duan, L.; Zhang, B.; Zhang, X.; Sun, T.; Wang, C.; Shi, Q.; Shang, W.; Shen, Y.; Lin, Z.; et al. Development of a Control Algorithm for a Hybrid Structure Surgical Manipulator. In Proceedings of the 2017 IEEE 7th Annual International Conference on CYBER Technology in Automation, Control, and Intelligent Systems (CYBER), Honolulu, HI, USA, 31 July–4 August 2017; pp. 1665–1670. [CrossRef]
27. Khan, H.; Kausar, Z.; Bari, S. Modeling and Analysis of Multi-Purpose Hybrid Surgical Robot. In Proceedings of the 2019 16th International Bhurban Conference on Applied Sciences and Technology (IBCAST), Islamabad, Pakistan, 8–12 January 2019; pp. 389–395. [CrossRef]
28. Liang, F.; Zhang, G.; Zhang, T.; Guan, Y.; Liu, G. Kinematics Analysis of a Hybrid Robot Consisting of a SCARA and a Parallel Wrist. In Proceedings of the 2019 IEEE International Conference on Robotics and Biomimetics (ROBIO), Dali, China, 6–8 December 2019; pp. 558–563. [CrossRef]
29. Saafi, H.; Laribi, M.A.; Zeghloul, S. Design of a 4-DoF (Degree of Freedom) Hybrid-Haptic Device for Laparoscopic Surgery. *Mech. Sci.* **2021**, *12*, 155–164. [CrossRef]

30. Feng, Y.; Chen, M.; Tao, B.X.; Wang, S.G.; Mo, J.Q.; Wu, Y.Q.; Liang, Q.H. A Self-Evolution Hybrid Robot for Dental Implant Surgery. In *Lecture Notes in Computer Science*; Springer: Cham, Switzerland, 2021; Volume 13015, pp. 93–102. [CrossRef]
31. Zheng, H.; Liang, C.; Gao, F.; Qi, C.; He, B.; Liu, R.; Chen, L. Design of a Novel Macro-Micro Integrated Brain Surgery Robot Based on Modular Parallel Mechanisms. *Chin. J. Mech. Eng.* **2024**, *37*, 130. [CrossRef]
32. Tucan, P.; Ciocan, A.; Gherman, B.; Radu, C.; Vaida, C.; Al Hajjar, N.; Chablat, D.; Pisla, D. Design Optimization of a Parallel Robot for Laparoscopic Pancreatic Surgery Using a Genetic Algorithm. *Appl. Sci.* **2025**, *15*, 4383. [CrossRef]
33. Lu, S.; Li, Y.; Ding, B. Kinematics and Dynamics Analysis of the 3PUS-PRU Parallel Mechanism Module Designed for a Novel 6-DOF Gantry Hybrid Machine Tool. *J. Mech. Sci. Technol.* **2020**, *34*, 345–357. [CrossRef]
34. Kizir, S.; BiNgül, Z. Design and Development of a Stewart Platform Assisted and Navigated Transsphenoidal Surgery. *Turk. J. Electr. Eng. Comput. Sci.* **2019**, *27*, 961–972. [CrossRef]
35. Hu, S.; Liu, H.; Kang, H.; Ouyang, P.; Liu, Z.; Cui, Z. High Precision Hybrid Torque Control for 4-DOF Redundant Parallel Robots under Variable Load. *Actuators* **2023**, *12*, 232. [CrossRef]
36. Jakobović, D.; Budin, L. Forward Kinematics of a Stewart Platform Mechanism. *Fac. Electr. Eng. Comput. Fac. Electr. Eng. Comput. Unska* **2002**, *3*, 10000.
37. Shah, M.F.; Kausar, Z.; Farooq, M.U. Kinematic Modeling and Analysis of a 6 Dof Parallel Machining Bed. In Proceedings of the 2019 22nd International Multitopic Conference (INMIC), Islamabad, Pakistan, 29–30 November 2019. [CrossRef]
38. Merlet, J.P.; Gosselin, C.; Huang, T. Parallel Mechanisms. In *Springer Handbooks*; Springer: Cham, Switzerland, 2016; pp. 443–462. [CrossRef]
39. Hussain, S.; Jamwal, P.K.; Van Vliet, P. Design Synthesis and Optimization of a 4-SPS Intrinsically Compliant Parallel Wrist Rehabilitation Robotic Orthosis. *J. Comput. Des. Eng.* **2021**, *8*, 1562–1575. [CrossRef]
40. Diao, X.; Ma, O.; Lu, Q. Singularity Analysis of Planar Cable-Driven Parallel Robots. In Proceedings of the 2008 IEEE Conference on Robotics, Automation and Mechatronics, Chengdu, China, 21–24 September 2008; pp. 272–277. [CrossRef]
41. Hussain, S.; Jamwal, P.K.; Kapsalyamov, A.; Ghayesh, M.H. Numerical Framework and Design Optimization of an Intrinsically Compliant 3-DOF Parallel Robot. *J. Comput. Inf. Sci. Eng.* **2021**, *21*, 021008. [CrossRef]
42. Kalsoom, A.; Farooq, S.S.; Shah, M.F.; Kausar, Z. Design Optimization of a Six Degrees of Freedom Parallel Mechanism Based Robotic Machining Bed. In Proceedings of the 2024 3rd International Conference on Emerging Trends in Electrical, Control, and Telecommunication Engineering (ETECTE), Lahore, Pakistan, 26–27 November 2024. [CrossRef]
43. Huang, T.; Gosselin, C.M.; Whitehouse, D.J.; Chetwynd, D.G. Analytical Approach for Optimal Design of a Type of Spherical Parallel Manipulator Using Dexterous Performance Indices. *Proc. Inst. Mech. Eng. Part C J. Mech. Eng. Sci.* **2003**, *217*, 447–456. [CrossRef]
44. Gosselin, C.M.; Lavoie, E. On the Kinematic Design of Spherical Three-Degree-of- Freedom Parallel Manipulators. *Int. J. Robot. Res.* **1993**, *12*, 394–402. [CrossRef]
45. Behzadipour, S.; Khajepour, A. Stiffness of Cable-Based Parallel Manipulators with Application to Stability Analysis. *J. Mech. Des.* **2006**, *128*, 303–310. [CrossRef]
46. Mollah, M.A.; Faizian, P.; Rahman, M.S.; Yuan, X.; Pakin, S.; Lang, M. A Comparative Study of Topology Design Approaches for HPC Interconnects. In Proceedings of the 2018 18th IEEE/ACM International Symposium on Cluster, Cloud and Grid Computing (CCGRID), Washington, DC, USA, 1–4 May 2018; pp. 392–401. [CrossRef]
47. Pisla, D.; Gherman, B.; Vaida, C.; Plitea, N. Kinematic Modelling of a 5-DOF Hybrid Parallel Robot for Laparoscopic Surgery. *Robotica* **2012**, *30*, 1095–1107. [CrossRef]
48. Evangeliou, N.; Tzes, A. A Hybrid Actuated Robotic Prototype for Minimally Invasive Surgery. In Proceedings of the 2018 IEEE International Conference on Robotics and Automation (ICRA), Brisbane, QLD, Australia, 21–25 May 2018; pp. 1386–1391. [CrossRef]
49. Leung, F.F.; Borvorntanajanya, K.; Chen, K.; Zari, E.; Garriga-Casanovas, A.; Franco, E.; Baena, F.R.Y.; Chiu, P.W.Y.; Yam, Y. Hybrid Manipulator with Force Estimation for Lower Gastrointestinal Interventions. *IEEE Robot. Autom. Lett.* **2024**, *9*, 9709–9716. [CrossRef]
50. Jamwal, P.K.; Kapsalyamov, A.; Hussain, S.; Ghayesh, M.H. Performance Based Design Optimization of an Intrinsically Compliant 6-Dof Parallel Robot. *Mech. Based Des. Struct. Mach.* **2022**, *50*, 1237–1252. [CrossRef]
51. Ma, H.; Zhang, Y.; Sun, S.; Liu, T.; Shan, Y. A Comprehensive Survey on NSGA-II for Multi-Objective Optimization and Applications. *Artif. Intell. Rev.* **2023**, *56*, 15217–15270. [CrossRef]
52. Pusey, J.; Fattah, A.; Agrawal, S.; Messina, E.; Jacoff, A. Design and Workspace Analysis of a 6-6 Cable-Suspended Parallel Robot. In Proceedings of the 2003 IEEE/RSJ International Conference on Intelligent Robots and Systems (IROS 2003) (Cat. No.03CH37453), Las Vegas, NV, USA, 27–31 October 2003; Volume 3, pp. 2090–2095. [CrossRef]
53. Stoica, A.; Pisla, D.; Andras, S.; Gherman, B.; Gyurka, B.Z.; Plitea, N. Kinematic, Workspace and Singularity Analysis of a New Parallel Robot Used in Minimally Invasive Surgery. *Front. Mech. Eng.* **2013**, *8*, 70–79. [CrossRef]

54. Zhao, H.; Yan, L.; Hou, Z.; Lin, J.; Zhao, Y.; Ji, Z.; Wang, Y. Error Analysis Strategy for Long-Term Correlated Network Systems: Generalized Nonlinear Stochastic Processes and Dual-Layer Filtering Architecture. *IEEE Internet Things J.* **2025**, *12*, 33731–33745. [CrossRef]
55. Ding, B.; Li, X.; Chen, S.C.; Li, Y. Modular Quasi-Zero-Stiffness Isolator Based on Compliant Constant-Force Mechanisms for Low-Frequency Vibration Isolation. *J. Vib. Control* **2024**, *30*, 3006–3020. [CrossRef]

Disclaimer/Publisher's Note: The statements, opinions and data contained in all publications are solely those of the individual author(s) and contributor(s) and not of MDPI and/or the editor(s). MDPI and/or the editor(s) disclaim responsibility for any injury to people or property resulting from any ideas, methods, instructions or products referred to in the content.